Department of Physics and Astronomy

University of Heidelberg

Master thesis in Physics

submitted by

Moritz Weegen

born in Langenfeld (Germany)

June 2018

Multiphoton Ionisation of Lithium from an optical Dipole Trap

This Master thesis has been carried out by Moritz Weegen at the
Max-Planck-Institute for Nuclear Physics under the supervision of
Priv.-Doz. Dr. Alexander Dorn

Zusammenfassung

Im Rahmen dieser Masterarbeit wurden Multiphotonionisationsprozesse an Lithium-6-Atomen aus einer optischen Dipolfalle untersucht und erstmals die Impulsverteilungen der resultierenden Ionen über den gesamten Raumwinkel in einem Reaktionsmikroskop ermittelt. Dabei wurden die Atome zunächst in einer magneto-optischen Falle präpariert, bevor sie in die rein optische Dipolfalle transferiert wurden. Es wurden Messungen für fünf verschiedene Intensitäten zwischen $6.5 \times 10^{13}\,\mathrm{W/cm^2}$ und $6.5 \times 10^{14}\,\mathrm{W/cm^2}$ durchgeführt, wobei ein Femtosekundenlaser als Projektilstrahl verwendet wurde. Die aus den Experimenten ermittelten Impulsverteilungen stimmen mit früheren vergleichbaren Messungen überein und bieten eine Basis für künftige Messungen.

Abstract

For this Master thesis, multiphoton ionisation processes of Lithium-6 atoms from an optical dipole trap have been investigated and the momentum distributions of the resulting ions over the whole solid angle in a Reaction Microscope have been obtained for the first time. The atoms have first been trapped in a magneto-optical trap, before being transferred into the purely optical dipole trap. Measurements for five different peak intensities in the range of $6.5 \times 10^{13}\,\mathrm{W/cm^2}$ to $6.5 \times 10^{14}\,\mathrm{W/cm^2}$ have been carried out, where a femtosecond laser has been used as the projectile beam. The experimentally obtained momentum distributions are consistent with formerly executed comparable experiments and offer a basis for future experiments.

Contents

1 Introduction

A deep understanding of the fundamental properties of atoms is of great importance for the understanding of the structure of our world and for global scientific development in general.
While learning more about the structures and dynamics of atoms can lead to new technical applications with the potential of changing global standards, as has been the case for the invention of the laser, there are also many other scientific fields that depend on a deep physical knowledge on atomic properties and behaviours such as chemistry, biology, material sciences, medicine and many more. In this sense, atomic physics is and has always been paving the way for further development of humankind.

Furthermore, the investigation on atomic physics never rests and there are many new and undiscovered fields at the current limits of atomic physics. New and more precise measurement techniques allow for the verification of formerly performed experiments, the validation or falsification of theoretical models or might even give rise to new questions and new phenoma yet to be explained.

One great field of interest is the investigation of ultra-cold atoms, especially quantum degenerate gases. Their preparation, however, is not trivial and gives rise to the motivation for this thesis. In order to obtain quantum degenerate gases, very low temperatures of just a few nK have to be reached, which is not possible by the use of conventional magneto-optical trapping techniques. Recently however, an optical dipole trap has been added to the experimental setup of a Reaction Microscope combined with a magneto-optical trap (MOTRemi) used within this thesis. These dipole traps provide

the necessary techniques to achieve the desired temperatures. The goal of this thesis is to obtain kinematically complete momentum distributions of ionisation processes from an optical dipole trap, as have not been obtained before.

For this purpose, Lithium-6 atoms were used as target atoms, as Lithium is a very instructive atom to study. It consists of a single valence elecron and can thus in certain approximations be seen as a hydrogen-like atom. Furthermore, its rather simple atomic energy level structure allows for a relatively easy trapping in magneto-optical traps, making it an ideal atomic species to start experiments with.

2 Theoretical Background

The following chapters aim to provide the necessary background knowledge behind the physical principles and the properties of the target atoms (^{6}Li) used within the experiments.

2.1 Laser Cooling by the Spontaneous Force

The cooling (and trapping) of neutral atoms is one of the most important experimental techniques in the field of fundamental atomic physics. The basic principle behind it is making use of the so-called *spontaneous force*. It is best understood by looking at a two level system:

Suppose an atom has the two distinct energy levels $|0\rangle$ and $|1\rangle$ with respective energies E_0 and E_1, as shown in figure 2.1. If such an atom finds itself in a light field consisting of photons with energy $E = E_1 - E_0$ and momentum $\vec{p} = \hbar\vec{k}$ (assuming $c = 1$), single photons can be absorbed and their energy and momentum are being transferred to the atom. The momentum transfer leads to a decrease of the atom's velocity (and thus of its temperature) if the light's direction is opposite to the respective velocity component of the atom. Since the atom will find itself in an excited state after the absorption of a photon, it will soon decay back into its ground state and emit another photon of the same energy. The momenta of these *spontaneously* emitted photons, however, are isotropically distributed, such that, averaged over many cycles, they do not affect the atom's momentum. This results in a net momentum transfer in the direction of the light field only. Additionally, stimulated emission from the light field can occure if the atom is in its excited state. But since in this case the emitted photons are coherent with the light field

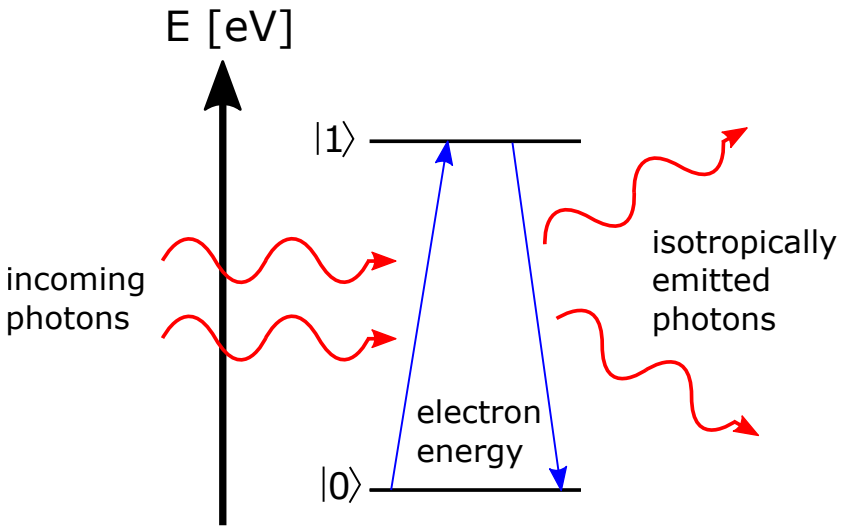

Figure 2.1: Schematic example of a two-level cooling process via spontaneous emission. Incoming laser light excites the atoms, before falling back into the ground state. The emitted light is isotropically distributed, resulting in a net momentum transfer in direction of the laser light.

and always show in the same direction, they do not induce any momentum change within the atom and are therefore negligible [1].

The resulting force of the induced spontaneous emission is called the *spontaneous force* F_{sp} and depends on the photons' momenta and the scattering rate γ_{sc}:

$$F_{sp} = \hbar \vec{k} \gamma_{sc} \tag{2.1}$$

Assuming a steady state situation, the scattering rate equals the rate of spontaneous emission γ from the excited state $\gamma_{sc} = \frac{1}{\tau}\rho_{ee}$, where $\tau = \frac{1}{\gamma}$ is the excited state's life time and ρ_{ee} its population [2][3]. By solving the stationary optical Bloch equation one finds the scattering rate to be given by [1]:

$$\gamma_{sc} = \frac{\gamma}{2} \frac{s_0}{1 + s_0 + (\frac{2\delta_0}{\gamma})^2} \tag{2.2}$$

Here, $s_0 = \frac{I}{I_s}$ is called the saturation parameter and defined as the ratio between laser intensity I and the saturation intensity I_s. I_s itself is defined as the necessary laser intensity to excite $\frac{1}{4}$ of the atoms in the laser field at a detuning of $\delta_0 = 0$ [4]. The detuning $\delta_0 = \omega_l - \omega_0$ is defined as the difference in frequency of the light field ω_l from the atomic resonance frequency ω_0.
In the high intensity limit $s_0 \to \infty$, the spontaneous force reaches its maximum at $F = \hbar\vec{k}\frac{\gamma}{2}$.

2.2 Doppler Cooling

In the previous chapter, the basic principles behind laser cooling via the spontaneous force have been explained. However, since the atoms are not at rest, the *Doppler effect* has to additionally be taken into account.
Atoms moving with a certain velocity $\vec{v}$ will "see" the laser field red- or blue-shifted, depending on their relative motion toward each other. This frequency shift can be taken into account by adding the term $\vec{k}\vec{v}$ to the total detuning of the laser field to the resonance frequency of the atomic transition in question, $\delta_0 = \omega_l - \omega_0 - \vec{k}\vec{v}$. The minus sign takes into account that opposite motion of atoms and light field leads to blue Doppler shifts. This additional term in the detuning of the system leads to a modified scattering rate of the atomic transition and to a velocity-dependent spontaneous force, given by:

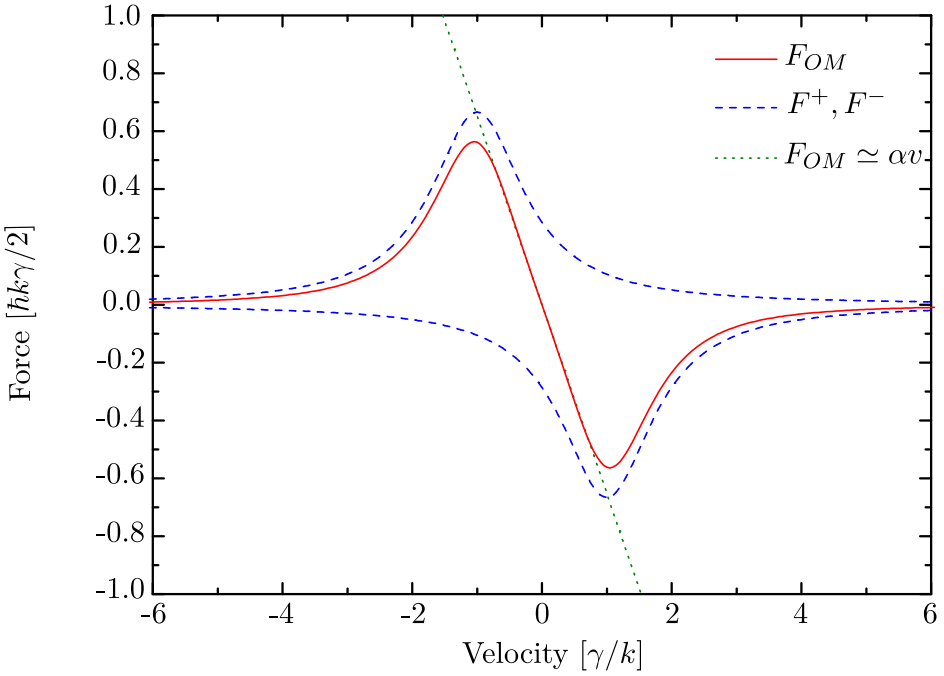

Figure 2.2: The spontaneous force F_{sp} on an atom against its velocity v. For small velocities, a linear approximation (green dashed line) is feasible. [2]

$$\vec{F}_{sp\pm} = \frac{\hbar\vec{k}}{2}\gamma\frac{s_0}{1+s_0+(\frac{2(\omega_l-\omega_0\mp\vec{k}\vec{v})}{\gamma})^2} \tag{2.3}$$

Here, $\pm$ indicates atoms moving opposite or in the same direction as the light field's photons, respectively. The overall resulting cooling force for atoms in a laser field is then given by the sum of the forces in both directions $\vec{F}_{cool} = \vec{F}_{sp+} + \vec{F}_{sp-}$. Figure 2.2 shows the strength of F_{cool} in one dimension as a function of the atomic velocity. In the low velocity regime, neglecting terms of order $(\frac{kv}{\gamma})^2$ and higher, the cooling force can be approximated by a linear function $F_{cool} \propto v$ [5].

By choosing a red-detuned laser light frequency ω_l with respect to the resonance frequency ω_0, it is assured that momentum transfer only occurs

for atoms moving opposite to the photon momenta and thus only leads to slowing of the atoms. Applying two overlapping counter propagating beams ensures a cooling of the atoms in one dimension for both possible initial velocity directions.
Since the atomic energy levels as well as the laser frequencies have a certain bandwidth, reactions will not only occur at the exact central resonance frequency, but over a certain range of frequencies with decreasing probability. Additionally to that, an increase in the light field's intensity will not only lead to higher scattering rates at a detuning of $\delta_0 = 0$, but also to higher reaction probabilities over an increasing detuning range, as shown in figure 2.3. This phenomenon is known as *power broadening* and makes the atoms more responsive for cooling at high laser intensities [6].

Experimental applications of this solely light-based cooling technique are called *optical molasses* and can lead to very low temperatures of the atoms in question.

2.3 Spacial Confinement of neutral Atoms

The application of laser cooling as presented in the previous chapters leads to an effective cooling of neutral atoms, i. e. to a reduction of their kinetic energy, which translates to their respective temperature via $k_B T = \frac{2}{3}\langle E_{kin}\rangle$, where $\langle E_{kin}\rangle$ is the average kinetic energy of the atomic ensemble [5].
This can be understood as a confinement of the atoms in *velocity* or *momentum space*. While it is important to cool and keep atoms at very low temperatures in order to achieve a good momentum resolution [7][8], in many applications an additional spacial confinement is desirable, by trapping atoms in a finite and small volume, acting as the reaction volume for later exper-

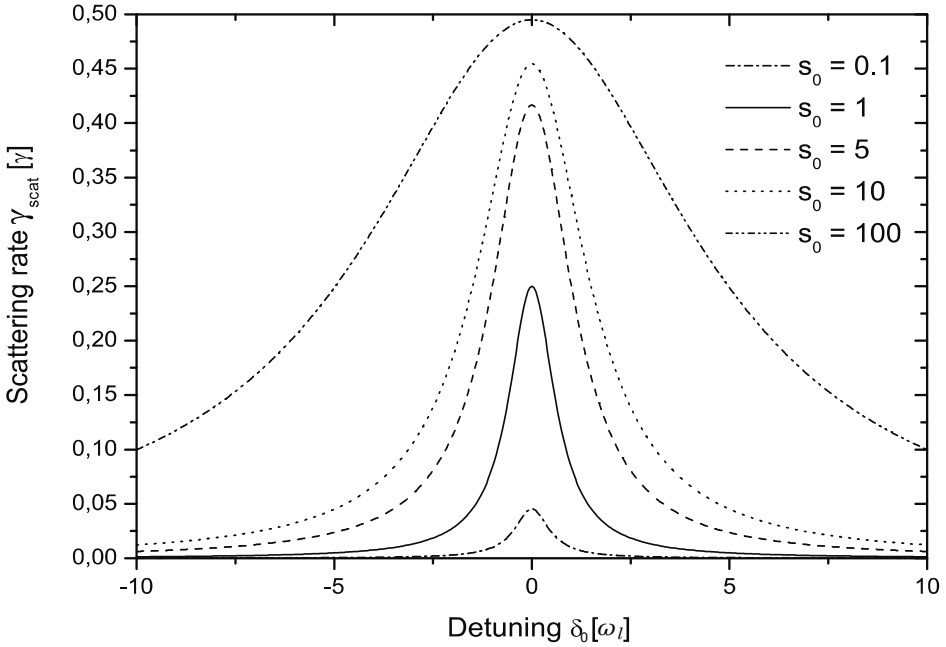

Figure 2.3: The scattering rate γ_{sc} as a function of the detuning δ_0 for different laser intensities. As one can see, a higher intensity not only increases the maximum scattering rate, but also the scattering probability over a wider range of detuning. [5]

iments. This can be achieved by applying an additional magnetic gradient field to the cooling laser field. In the following, the working principles of this spacial confinement will be discussed, considering only one dimension of atomic motion.

Consider a neutral atom with its motion restricted on the z-axis, being cooled by two counter propagating red-detuned laser fields as shown in figure 2.4. Assuming a total angular momentum of $F = 0$ for the atom's ground state $|0\rangle$ and a total angular momentum of $F = 1$ for its excited state $|1\rangle$, adding a magnetic $\vec{B}$-field to the system will result in a fine structure splitting of the $|1\rangle$ state into 3 energy sublevels with angular momentum z-components given

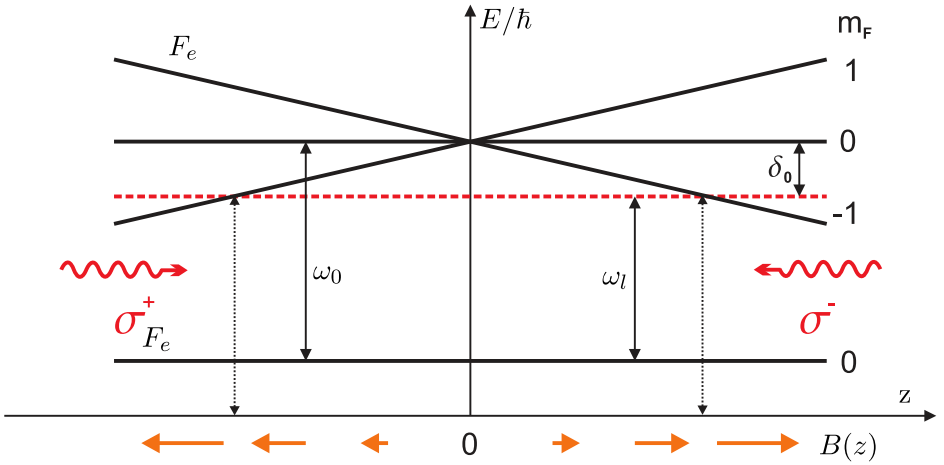

Figure 2.4: Working principle of a one-dimensional magneto-optical trap. Red-detuned laser light with correct helicity in a gradient magnetic field allows for a space-dependent cooling force and spacial confinement of the atom. [1]

by the quantum numbers $m_F = 0$ and $m_F = \pm 1$ due to the *Zeeman effect* [5]. The strength of this splitting is directly correlated to the strength of the applied magnetic field, i. e. a gradient $\vec{B}$-field will lead to a space-dependent splitting of the energy levels, as can be seen in figure 2.4. By choosing solely circularly polarised $\sigma_\pm$ light beams, transitions can be restricted to excite into the $|1\rangle_{m_{F=\pm1}}$ states, thus completely suppressing any transitions to $|1\rangle_{m_{F=0}}$, which requires π^0 polarised light and shows no space-dependece. This leads to an additional term $\frac{\Delta\mu B(z)}{\hbar}$ in the detuning δ_0, now given by:

$$\delta_{0\pm} = \omega_l - \omega_0 \mp \vec{k}\vec{v} \pm \frac{\Delta\mu B(z)}{\hbar} \tag{2.4}$$

As a side effect, the cooling of atoms via induced momentum transfer from a light field additionally leads to a heating rate of the atoms, effectively setting

a limit on the achievable minimum temperature of the system. This heating rate is given by [1]

$$\dot{E}_{heat} = \frac{1}{2m}\frac{d}{dt}\langle p^2 \rangle \tag{2.5}$$

and results in the so-called *Doppler limit* for the achievable temperature:

$$T_D(\delta) = \frac{\hbar\gamma}{4k_B}\frac{1 + (2\delta/\gamma)^2}{(|\delta|/\gamma)} \tag{2.6}$$

As a function of the detuning, the Doppler limit reaches its absolute theoretical minimum at $\delta = -\frac{\gamma}{2}$:

$$T_D(-\frac{\gamma}{2}) = \frac{\hbar\gamma}{2k_B} \tag{2.7}$$

2.4 Optical Trapping in a Dipole Trap

The cooling and trapping of atoms with Doppler cooling is an adequate technique in order to achieve temperatures of the order of magnitude of $\approx$100 μK [6]. Unfortunately this is not sufficiently cold for the creation of quantum degenerate Fermi gases which require temperatures of just a few nK [9]. However, making use of Doppler cooling, e. g. in the implementation of a *Magneto-Optical Trap* (MOT), as has been the case for this thesis (see also chapter 3.4), is a good starting point for achieving the desired temperatures in a second step.

The further cooling of the trapped atoms in this thesis has been realised by the implementation of a so-called optical *Dipole Trap*. It is realised by adding a far red-detuned laser field to the already pre-cooled atoms. The main interaction of this laser field with the atoms is not via any momentum exchange, but rather via the creation of a conservative potential through the interaction of its electric field with the induced electric dipole of the atoms [1]. The basic principles of such an optical trap can best be unterstood by looking at a simplified classical model:
The electric field from the laser light interacting with the atoms is given by:

$$\vec{E}(\vec{r},t) = \vec{\epsilon}\hat{E}(\vec{r})e^{-i\omega t} + c.c. \tag{2.8}$$

$\vec{\epsilon}$ is the unit polarisation vector, $\hat{E}$ the light field's amplitude and ω its driving frequency. The term "*c.c.*" denotes the *complex conjugate* of the first term. Similarly, the induced atomic dipole moment is given by:

$$\vec{p}(\vec{r},t) = \vec{\epsilon}\hat{p}(\vec{r})e^{-i\omega t} + c.c. \tag{2.9}$$

For red-detuned light, the resulting interaction leads to an attractive potential with its depth given by:

$$U_{dip}(\vec{r}) = -\frac{3\pi c^2}{2\hbar\omega_0^3}(\frac{\Gamma}{\omega_0-\omega} + \frac{\Gamma}{\omega_0+\omega})I(\vec{r}) \tag{2.10}$$

Here, Γ is the line width of the atomic transition, ω_0 its frequency and $I(\vec{r})$ the intensity of the dipole laser light.
Since the atoms pre-cooled via Doppler cooling do not all have the same kinetic energy, but instead follow a certain velocity/temperature distribution

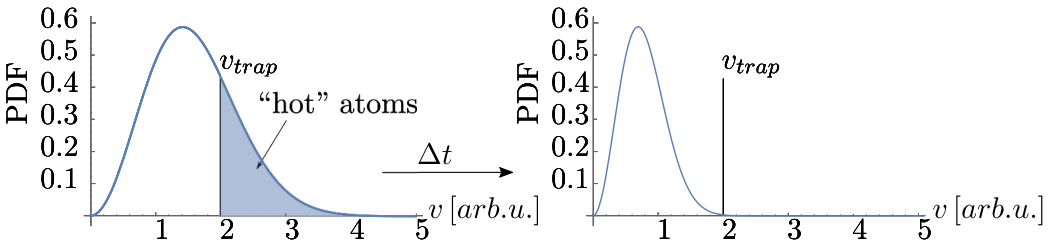

Figure 2.5: Principle behind the transfer of atoms from a MOT into a dipole trap and evaporative cooling. By applying a conservative potential, too "hot" atoms with kinetic energies exceeding the potential barrier will be lost. After a certain time the remaining atoms rethermalise into a new Maxwell-Boltzmann distribution. [1]

(the *Maxwell-Boltzmann distribution*, see also chapter 2.5 for more detailed information), applying a dipole trap will result in the trapping of only a fraction of the pre-cooled atoms, namely the ones with insufficiently high kinetic energies to overcome the potential barrier induced by the conservative dipole potential. By disabling Doppler cooling while a dipole laser field is applied to the atoms, all atoms with higher kinetic energy will thus quickly leave the trapping volume, such that only a small, but remarkably colder fraction of the pre-cooled atoms remains in the trapping region for further experiments. These atoms will then again rethermalise and follow another Maxwell-Boltzmann distribution with lower average kinetic energy, as can schematically be seen in figure 2.5.

Besides the capability of reaching much lower temperatures than a trap relying on Doppler cooling, another crucial advantage of an optical dipole trap is the absence of a magnetic field, since it is not anymore needed in order to create a spacially confining force. In general, especially in ionisation experiments, external magnetic fields are undesirable and should be reduced

to a minimum since they influence the motion of charged particles. A further advantage is that all of the atoms in a dipole trap are in their ground state, such that no mix states emerge and the target properties are very well known.

2.5 Evaporative Cooling

As already mentioned in the previous chapter, the velocities v of the atoms with mass m trapped in a dipole trap follow a Maxwell-Boltzmann distribution [5], given by:

$$p(v) = \sqrt{(\frac{m}{2\pi k_B T})^3} 4\pi v^2 e^{-\frac{mv^2}{2k_B T}} \tag{2.11}$$

One such distribution can be seen in figure 2.6.

In a Maxwell-Boltzmann distribution, the velocity at the distribution's maximum $v_{max} = \sqrt{2\frac{k_B T}{m}}$ differs from the average velocity $\langle v \rangle = \frac{2}{\sqrt{\pi}} v_{max}$. The latter gives rise to the emsemble's average temperature via $k_B T = \frac{2}{3}\langle E_{kin} \rangle$

After the transfer of the atoms from a Magneto-Optical-Trap into a dipole trap as described in chapter 2.4, further cooling can be achieved by the technique of *evaporative cooling*. The principles behind it are simple:

When thermal equilibrium of the atoms in the dipole trap is reached, the trapping depth of the dipole potential needs to be decreased, such that a shift of the maximum trapping velocity v_{trap} toward lower velocities (i. e. lower temperatures) occurs. This can practically be achieved by lowering the dipole laser intensity.

As a consequence, the fastest atoms initially trapped in the dipole trap will no longer be confined to the trapping volume, since they are now able to overcome the potential barrier. This "cut off" of the highest energetic atoms

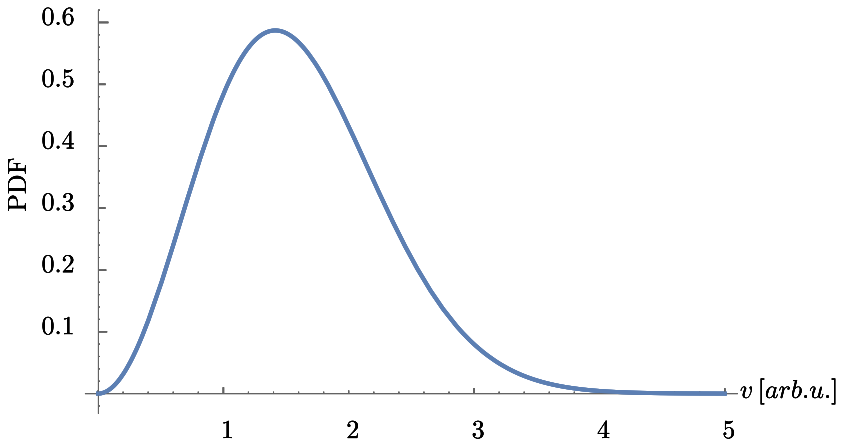

Figure 2.6: Example of a Maxwell-Boltzmann distribution as followed by the evaporated atomic ensembles used within the experimental setup. The distribution is a probability density function (PDF) of the single atomic velocities of the ensemble. [1]

in the trap leads to a rethermalisation of the remaining atoms into another Maxwell-Boltzmann distribution, similar to the transfer of atoms from a MOT into a dipole trap (see figure 2.5 and chapter 2.4). While the atomic ensemble in this resulting distribution has a lower average temperature, it comes at the cost of a decreased atom number within the trapping volume. By repeating this process several times, very low temperatures in the order of magnitude of 100 nK can be reached [9], sufficiently low for the creation and study of quantum degenerate gases such as *Bose-Einstein condensates* (BEC).

2.6 Photoionisation of Atoms

In the following chapters, the kinematics behind single and multiphoton ionisation processes will be discussed. Since the photon energies of the projectiles

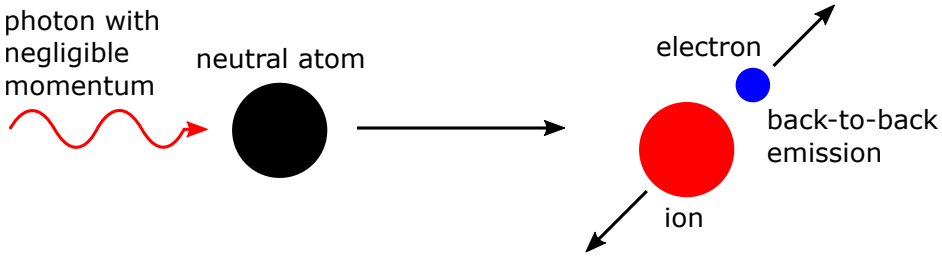

Figure 2.7: Schematic of a single photoionisation process. A single photon hitting a neutral atom results in a back-to-back ejection of the produced ion and electron due to the negligible photon momentum.

used for the experiments were not sufficiently high to remove electrons from the atoms' inner shells, we will only consider the ionisation of valence electrons.

2.6.1 Single Photoionisation

In the process of *single photoionisation* the momentum and energy of a *single* photon is being transferred to one of an atom's electrons, as schematically shown in figure 2.7. This will only lead to ionisation of the atom if the photon energy $E_{ph} = \hbar\omega_l$ exceeds the atom's ionisation potential E_{IP}. Since the photon is being absorbed in this process, a rather simple kinematic two-body problem results, consisting of the ejected electron and the ionised atom.
Due to the much higher mass of the ion in comparison with the electron (the ratio of these is already roughly 2000 for hydrogen, the lightest of all elements), it is justified to neglect the resulting kinetic energy of the ion for further calculations and assume that the whole excess energy $E = E_{ph} - E_{IP}$ corresponds to the electron's kinetic energy E_{kin}.
Furthermore, in all experiments discussed within this thesis, the absolute

momenta of the ionising photons p_{ph} were much smaller than the resulting momenta of each one of the interaction particles, such that the photons' momenta can be neglected.

Of course, the overall momentum still has to be preserved, such that assuming $p_{ph} \approx 0$ leads to a back-to-back ejection of the electrons with respect to the recoil ions, i. e. $\vec{p_e} = -\vec{p_r}$ [3]. The final absolute momenta of the electrons/ions are then determined by the kinetic energy transfer from the photons to the electrons:

$$p_e = p_r = \sqrt{2m_e E_{kin}} \tag{2.12}$$

Due to the process being reduced to a two-body problem, the resulting momentum and energy transfer is well defined, such that all momenta of involved particles in ionisation events must lie on a sphere of radius $p = \sqrt{2m_e E_{kin}}$ in three-dimensional momentum space [10]. The spacial/angular ejection distribution of the particles, however, is generally not isotropical and depends for example on the polarisation of the ionising laser light field and the state from which an electron is ejected [3].

Furthermore, the detection of either electrons or ions alone yields principally enough information to deduce the corresponding momentum distribution of the other type of particle, since they only differ by a change of sign. Since ions are generally less prone to deflections due to external fields, they are generally easier to detect.

2.6.2 Multiphoton Ionisation

Opposed to single photoionisation, in which case a single photon energy of $E_{ph} - E_{IP} \geq 0$ is necessary, it is possible to ionise atoms with several consecutive hits of photons of energies $E_{ph} - E_{IP} < 0$, as long as the sum of their energies exceeds the ionisation potential [7]. This means, for an integer number N, multiphoton ionisation can principally occur when $NE_{ph} - E_{IP} \geq 0$. Typically this is not possible for a single well-defined photon energy, since electrons can only be excited to other discrete and well-defined energy levels within an atom that are not evenly separated. However, if the time difference between consecutive photon hits is short enough, electrons can be excited to *virtual states*, consistent with Heisenberg's uncertainty relation $\Delta E \Delta t \geq \frac{\hbar}{2}$ [11]. These virtual states may lie between the real energy levels of an atom, as shown in figure 2.8.

Multiphoton ionisation can be realised by using a *femtosecond laser* with ultra-short pulses and is a non-linear process, i. e. the probability for a multiphoton ionisation event does not scale linearly with the light field's intensity, as opposed to single photoionisation.

Furthermore, it is possible for atoms to absorb more photons than necessary for ionisation and transfer their energy and momenta on a single electron. This process is called *above threshold ionisation* [3] and yields time of flight spectra as shown in figure 2.9.

2.7 Properties of Lithium-6

Lithium is the lightest of all metals with an atomic number/proton number of 3 in the table of the elements. As it consists of one valence electron in its

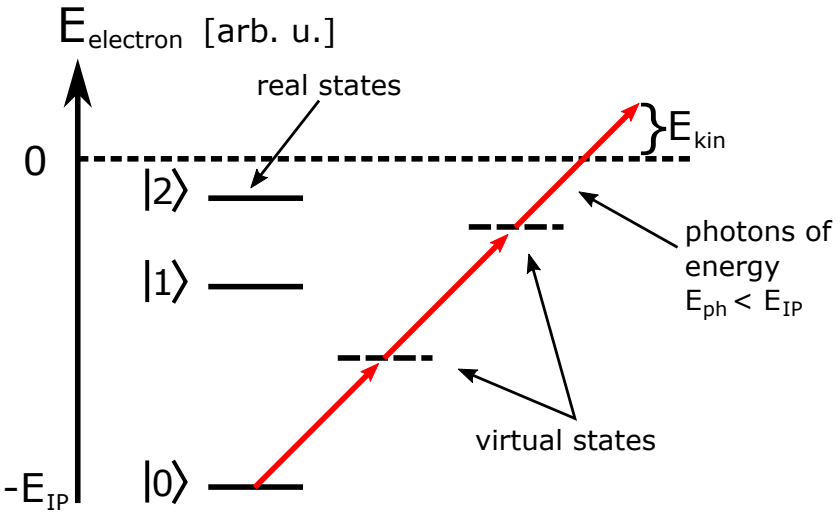

Figure 2.8: Example energy level diagram for a multiphoton ionisation process. Even though any single photon is not in resonance with the real atomic energy levels, they can consecutively excite the atom to virtual states and ultimately ionise it by exceeding the ionisation energy.

outer shell, it is part of the group of the alkali metals and highly reactive. The fundamental atomic properties of the ^{6}Li isotope are listed in table 2.1.

In its ground state, two electrons fully occupy the innermost $1S$ shell, while the valence electron is located in the $2^2S_{1/2}$ state. Since only ionisation from the valence electron has been investigated in this thesis and the $1S$ electrons stayed unaffected, we will solely focus on Lithium's atomic and optic properties with respect to the possible valence electron transitions.
The ionisation energy for ground state Lithium is given by $E_{IP} = 5.39\,\mathrm{eV}$ and its first excited $2P$ state's energy level is found at $-3.54\,\mathrm{eV}$ with respect to the continuum [10], as shown in figure 2.10. The transition from the $2S$

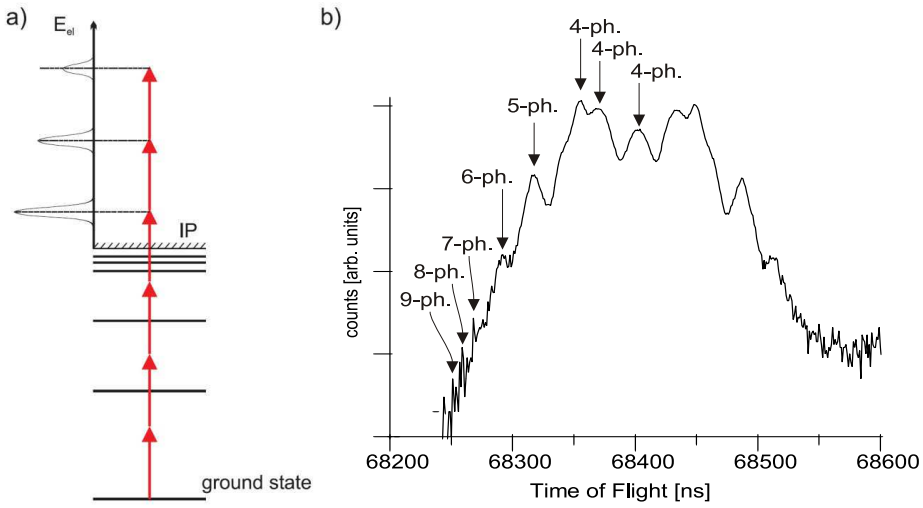

Figure 2.9: a) Example energy level diagram for above threshold ionisation. b)Time of flight spectrum for above threshold ionisation on a logarithmic scale. The peaks pointed out in the spectrum arise from the different kinetic energies of the ions due to above threshold ionisation with different amounts of photons ionising above the continuum threshold. [3]

to the $2P$ state is called the *D-line* of Lithium for historical reasons and is of major interest for this thesis, as it is used for the preparation of the Lithium target in a magneto-optical trap (see also chapter 3.4).

The energy levels shown in figure 2.10, however, do not take into account the fine and hyperfine structure of Lithium. These can be seen in figure 2.11. Since the $2P$ state corresponds to an angular electron momentum quantum number of $l = 1$, there are two possible alignments with the intrinsic electron spin of $s = \frac{1}{2}$, giving rise to the $2^2P_{1/2}$ and $2^2P_{3/2}$ states at the *D1* and *D2*-line transitions at wavelengths of 670.979 nm and 670.977 nm, respectively [14].

Property	Symbol	Value	Ref.
Atomic Number	Z	3	
Nucleons	$Z + N$	6	
Natural Abundance	η	7.6%	[12]
Nuclear Lifetime	τ	stable	[12]
Atomic Mass	m	$6.015\,121\,4\,\mathrm{u} = 9.988\,341 \times 10^{-27}\,\mathrm{kg}$	[13]
Total Electronic Spin	S	1/2	
Total Nuclear Spin	I	1	

Table 2.1: Fundamental atomic properties of Lithium-6. [14]

The hyperfine structure arises from the Lithium's nuclear spin quantum number $I = 1$.

In order to trap Lithium atoms in a MOT, it is necessary to precisely know its hyper fine energy levels and to prepare the lasers accordingly. In this thesis, the cooling and trapping was realised with D2-line transitions, as will be explained in more detail in chapter 3.4.

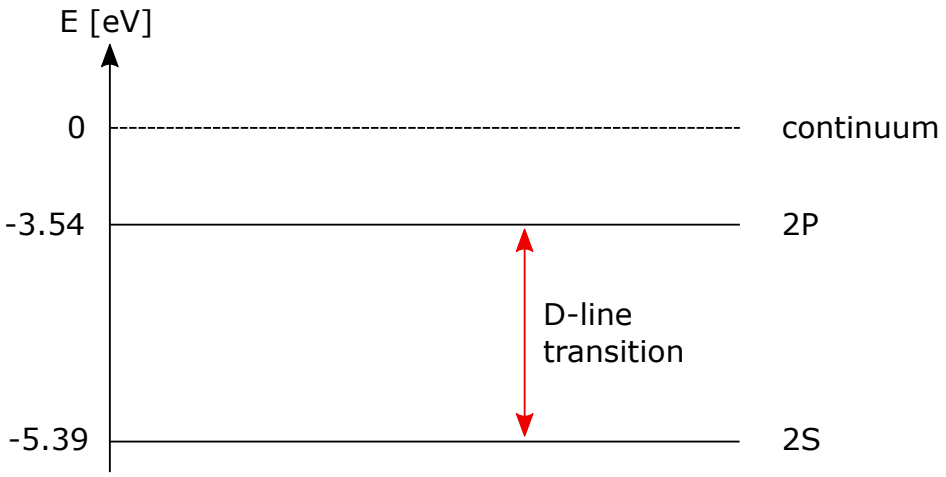

Figure 2.10: Simple energy level diagram of the $2S$ ground state and $2P$ excited state of ^{6}Li. Fine and hyperfine structure splitting is not shown in this diagram.

3 Experimental Setup

This chapter is aiming to provide a detailed overview on the experimental setup and its most important components and features as used within the experiments.

3.1 Reaction Microscopes

The experiment itself is set up in a so-called *Reaction Microscope* combined with a *magneto-optical trap*, as shown in Figure 3.1.

A Reaction Microscope is a state-of-the-art experimental setup for the detection of ions and electrons produced in ionisation processes [5]. Making use of the fundamental behaviours of charged particles in electric and magnetic fields, Reaction Microscopes allow for complete kinematic reconstructions of

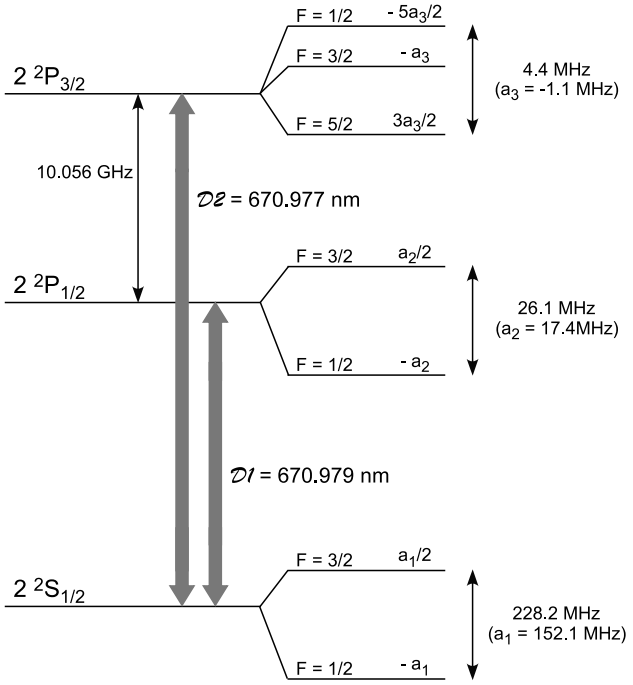

Figure 2.11: Fine and hyperfine structure of the 2^2S and 2^2P states of ^{6}Li. [14]

the involved particles' momenta at the time of ionisation and the *Fully Differential Cross Sections* (FDCS) of the corresponding interaction processes over the full solid angle [16], while solely relying on time measurements.

To achieve this, a spectrometer consisting of several ring electrodes is centred around the point of incident of the ionisation, giving rise to a cylindrical symmetry around the z-axis, therefore also referred to as the *spectrometer axis*. By applying steady potential differences between two consecutive ring electrodes, a nearly homogeneous electric field is being created within the spectrometer, separating ions and electrons produced in ionisation processes due to their opposite signs in charge. While ions will be accelerated towards negative values of z within this *Acceleration Region*, the opposite is the case for electrons [17].

After leaving the electric field procuded by the spectrometer, the particles

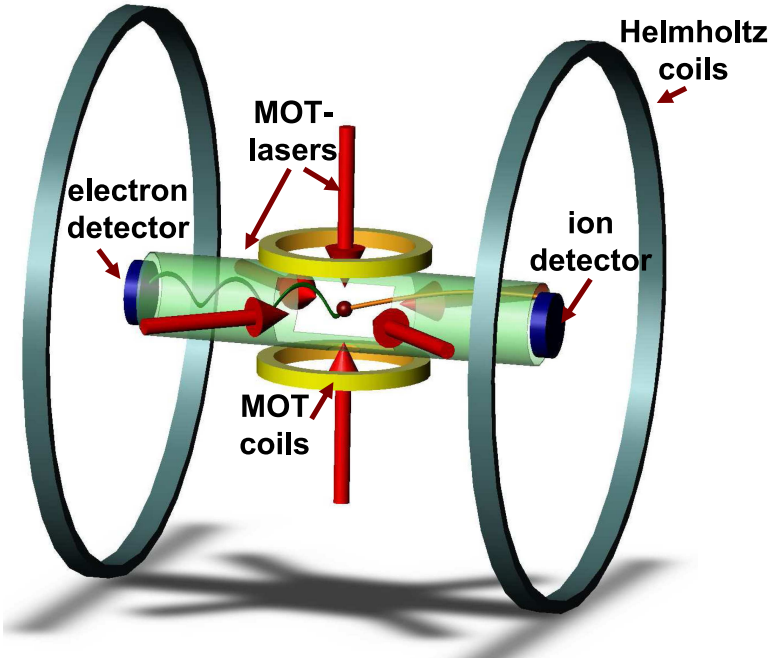

Figure 3.1: Technical image of a Reaction Microscope combined with a magneto-optical trap (MOT). The green cylindrical part in the centre shows the spectrometer responsible for the homogeneous electric extraction field, while the large Helmholtz coils produce the homogeneous magnetic field. Electrons and ions produced in the centre get accelerated towards their respective detectors in opposite directions. [15]

pass a field free region on either side of the Reaction Microscope in which they travel with constant velocity, before hitting position sensitive *Delay Line Anode* detectors centred around the spectrometer axis. These *Drift Regions* allow for a wider spreading of the particles' positions on the detectors, making events easier to distinguish and thus leading to a higher resolution for the reconstructed momenta.

Due to the relatively high masses of the scattered ions, their initial transversal velocities from the ionisation processes will be too low to get lost before

hitting the detector. However, this is not the case for the electrons, a majority of which would simply miss the detecor or hit the spectrometer because of their high velocities in transversal direction. In order to prevent this, two large Helmholtz coils are positioned around the spectrometer axis, providing a nearly homogeneous magnetic field in z-direction. This way the scattered particles are forced on cyclotron motions via the Lorentz force, keeping them inside the region of interest [18]. While the effect of this additional $\vec{B}$-field on the ions usually is negligible, the electrons will traverse several cyclotron trajectories before hitting the detector, leading to distorted position information that has to be taken into account for the momentum reconstruction.

3.1.1 The Spectrometer

As already mentioned in chapter 3.1, the spectrometer is positioned in the centre of the experimental setup, surrounding the point of incident of the observed ionisation processes. A schematic drawing of the spectrometer can be seen in figure 3.2.

Its main feature are the 19 middle ring electrodes in the Acceleration Region, providing a homogeneous electric field to separate the produced ions and electrons, also giving rise to a cylindrical symmetry. These 19 electrodes are pairwise connected via 18 kΩ resistors, such that applying a potential difference between the first and the last electrode of the Acceleration Region will result in a nearly uniform potential change within the whole region. In order to make the spectrometer centre accessible for target atoms and projectile lasers, the 17 centre-most electrodes have rectangular openings of a total size of 30 mm $\times$ 200 mm in the x-z-plane.

On the electron detector side, the spectrometer is directly extended by a

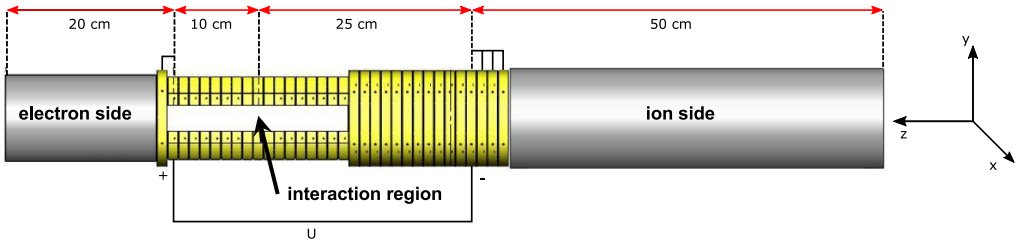

Figure 3.2: Sketch of the side view on the spectrometer used within the Reaction Microscope for the production of a homogeneous electric extraction field. The centre-to-centre distance between two consecutive electrodes was 1.25 cm with a 1 mm gap between them.

so-called *Drift Tube*. This is a simple metal tube, put on the same potential as the first electrode to provide the field free Drift Region for the electrons. On the ion side, however, before a similar Drift Tube is being applied, the spectrometer is extended by 14 additional ring electrodes, the last three of which are directly connected. These electrodes can individually be put on desired potentials, e. g. in order to extend the length of the Acceleration Region on the ion detector side. Furthermore, these additional electrodes allow for the mounting of *Electrostatic Lenses* [5]).

Two consecutive electrodes of the spectrometer have a distance of 1.25 cm, measured from centre-to-centre. Overall, the lengths of the acceleration (a) and drift regions (d) within the experiments discussed in this thesis were:

- a_r =25 cm
- d_r =50 cm

- a_e =10 cm
- d_e =20 cm

Here and in the following, the indices r and e refer to *recoil ions* and *electrons*, respectively.

3.2 The Detectors

Both the electron and ion detector are so-called *Delay Line Anode* detectors [19] centred around the spectrometer axis. They consist of *Micro-Channel Plates* (*MCPs*), followed by the actual Delay Line Anode, as can be schematically seen in figure 3.3. While the MCPs task is to produce detectable electron cascades out of the incoming scattered ions or electrons from the experiment, the Delay Line Anodes provide the necessary position information to reconstruct the particles' initial momenta, by relying on time measurements only [20].

In order to ensure a correct voltage supply for the different parts of the detectors, *signal boxes* are used, being especially built for this purpose. These boxes basically consist of voltage dividers that distribute the desired voltage fractions of an applied high voltage U_0 to the different detector parts. U_0 typically lies at around 2.5 kV to 2.7 kV.

Additionally to that, the final particle signals on the MCPs and delay line layers can be taken directly from the signal box.

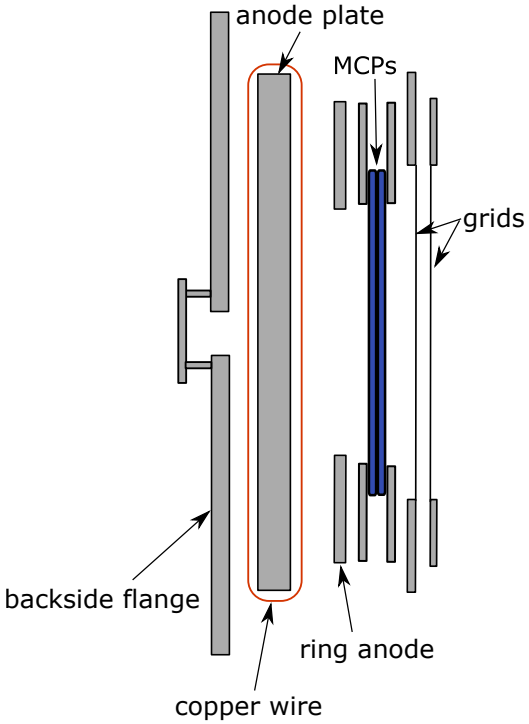

Figure 3.3: Schematic profile view on the position-sensitive delay line detectors used for the detection of ions and electrons. The single parts are supplied with the necessary voltages via especially built signal boxes. [20]

3.2.1 Micro-Channel Plates

The Micro-Channel Plates used for the detectors in this thesis are discs riddled with several holes, tilted by around 8° with respect to the MCPs surface, as can be seen in figure 3.4. Each of these holes (the *micro channels*) has a diameter of around 10 μm, while the whole MCPs diameter is 80 mm.
By applying a high voltage difference of some kV between the two surfaces, MCPs are capable of producing electron cascades out of incoming particles. When an incoming particle hits the wall of one of the micro channels, several electrons can be released which then again are being accelerated toward

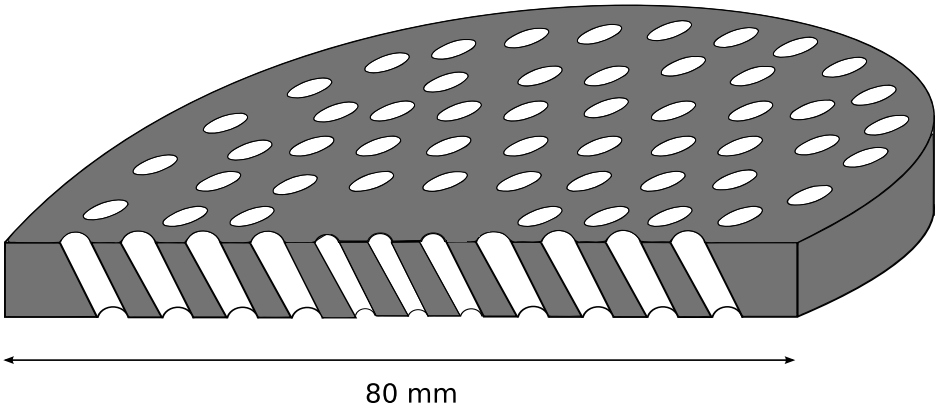

Figure 3.4: Drawing of an MCP used for the delay line detectors. The single micro channels are capable of producing electron clouds at an amplification of order of magnitude 10^6, creating a detectable signal on the delay lines. Note that the MCPs are full discs and not cut through as shown in the picture. [20]

the backside of the MCP. These electrons are then capable of repeating this process by hitting the walls once more. Overall, an electron amplification of order of magnitude 10^6 leads to a large detactable electron cascade within the microchannels, as schematically shown in figure 3.5. The voltage drop induced by this process can be measured and the resulting signal can be used to determine the arrival time of the particle in question. While the tilt of the micro channels with respect to the MCP's surface results in a higher electron multiplication, stacking two MCPs of opposing orientation in a so-called *Chevron* setup increases this effect even more. Additionally, this setup reduces the probability of *Feedback Ions* leaving the front side of the MCP stack [21].

This whole process leads to an electron cloud leaving the MCP back side and being able to create a sufficiently high signal on the following Delay Line Anodes behind the MCPs. However, since the micro channels only make up

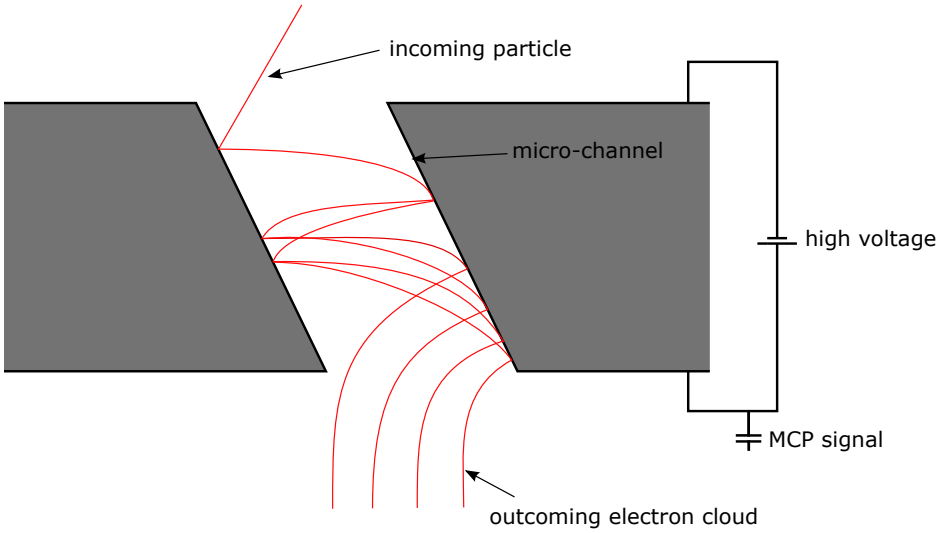

Figure 3.5: Working princple of a single micro channel of an MCP. The tilt of the channels with respect to the MCP surface increases the efficiency of creating an electron cascade. [20]

a fraction of the surface of a channel plate, there is a natural limitation on the detection efficiency of incoming particles of around 50 %.

3.2.2 Delay Line Anodes

Delay Line Anodes are position sensitive detectors typically used within Reaction Microscope setups that rely on simple time measurements for the determination of the arriving position of the particles, which will be used for further computation of their initial momenta.

While there are different setups for Delay Line Anode Detectors, the most simple design consists of two perpendicular layers of copper wiring for the two spacial dimensions x and y, wound around a steel plate and insulated with ceramics on the steel plate's edges. Electron clouds emerging from the

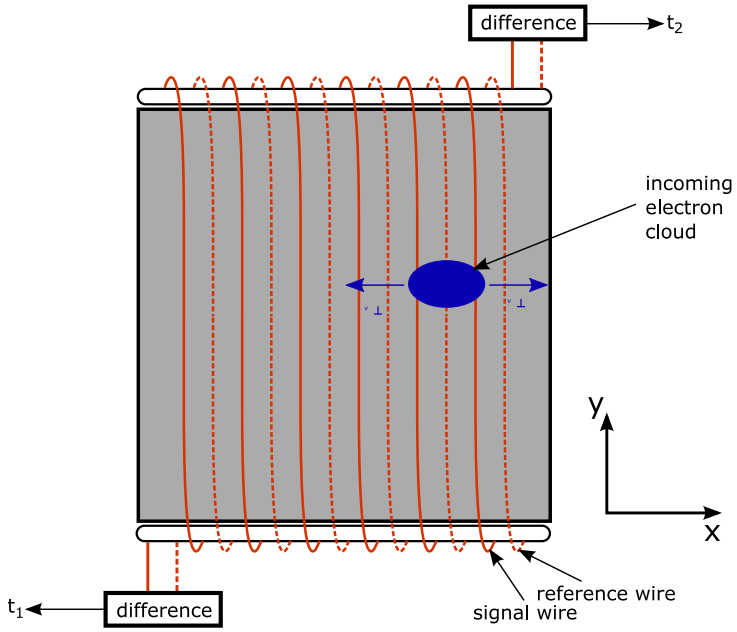

Figure 3.6: Working principle of a single delay line anode layer. Electron clouds hitting the copper wires induce signals that can be detected at both wire ends. From their respective travel times the incident position can be determined. Signal and reference wire allow for the subtraction of noise signals by taking the signal differences. [20]

MCPs and hitting the Delay Line Anode will give rise to a detectable signal on each layer, as schematically shown in figure 3.6. The signal will move toward both ends of a layer's cupper wiring, enabling the determination of their arrival times t_1 and t_2.

Considering only one dimension for the moment, the coordinates of the incident particle can be determined via the equation:

$$x = v_\perp((t_1 - t_0) - (t_2 - t_0)) = v_\perp(t_1 - t_2) \tag{3.1}$$

and for y respetively.

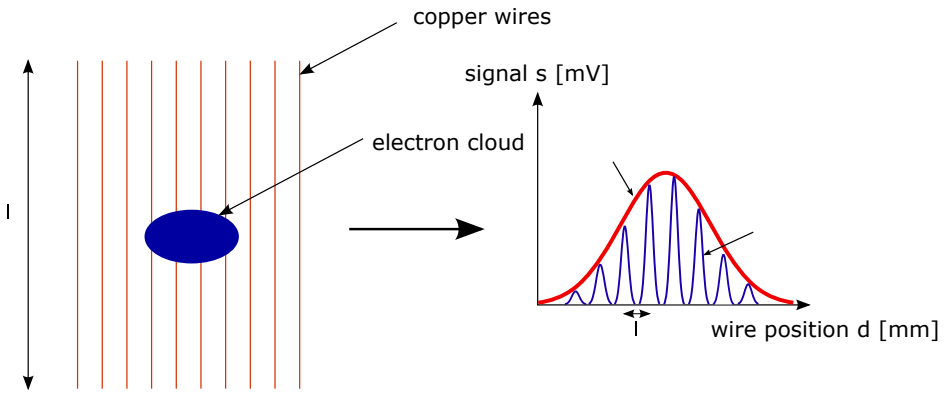

Figure 3.7: The detector resolution is not limited to the spacing of its wire layers, because the enveloping function of hits on different positions corresponds to the signal being observed. [20]

Here, $v_\perp$ is the velocity of the signal perpendicular to the wiring and t_1 and t_2 are the arrival times of the signal on both wire endings, relative to the MCP signal time t_0. $v_\perp$ is not necessarily precisely known, but its correct numerical value is not of importance for the further determination of the particles' momenta, since every delay line anode layer can be scaled correctly by shining out the complete MCP surface with a continuous isotropical source of particles.

Even though the copper wiring leads to a discrete grid of wires with a typical distance of around Δx =0.5 mm on each coordiante layer, the actual position resolution of the detectors is not limited to this value [22]. This is due to the fact that an electron cloud coming from the MCPs has a sufficiently large spreading to hit several windings of a layer, each of which giving rise to a small signal. However, the final signal being detected for the determination of the arrival times is the enveloping function of the signals, as shown in figure 3.7. This way, the centre of mass position of the electron cloud can be determined, which is not anymore restricted to the discrete wiring positions.

Another important feature of Delay Line Anode detectors is the *time sum condition*. It states that the time sum

$$t_{sum} = t_1 + t_2 - 2t_0 = const. \tag{3.2}$$

for the signal of a legitimate incident particle event is always constant. This can be used to distinguish real detector counts from dark counts or generally any other falsefully detected counts.

It is also important to note that each layer of a Delay-Line-Anode actually consists of two wires, a *signal wire* and a *reference wire*. The reference wire is set on a slightly lower voltage than the signal wire, such that a larger fraction of the electron clouds coming from the MCPs will hit the signal wires. This way, the difference between the signals on both wires can be taken for futher data processing (see figure 3.6). Since any background or noise signals should be roughly the same on each of the wires, taking the signal difference cancels out most of these undesired signals.

3.2.3 Hexanodes

While the two-dimensional Delay Line Anode design is typically used for the detection of ions, the detection of electrons proves to be generally more challenging. Therefore, the electron side of Reaction Microscopes typically features Delay Line *Hexanodes*.

The name of the Hexanodes arises from the use of three copper wiring layers with a respective angle of 60° toward each other (see figure 3.8), leading to a hexagon shape, but their working principles are the same as for the two-layer Delay Line Anodes. The main purpose of a third layer is to achieve an

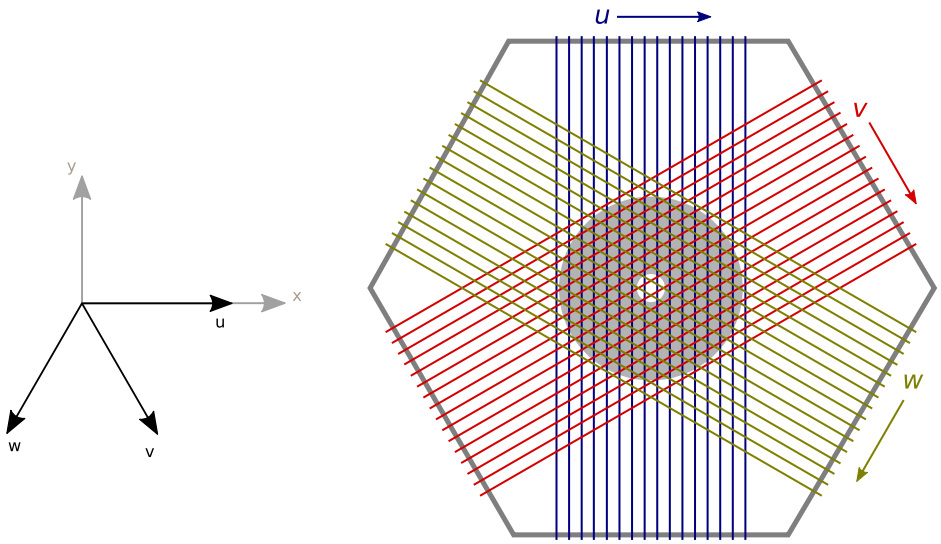

Figure 3.8: Drawing of a delay line hexanode. Hexanodes consist of three layers of copper wire, giving rise to three dependent coordinates u, v and w for the determination of x and y, corresponding to the coordinate system shown in the image. [22]

increased detection efficiency by introducing an additional degree of freedom for the detection of electrons. Since two-dimensional position information can only be retrieved if at least two layers yield time information from the electrons, a third layer acts as additional safety to gain complete position information if one of the other two layers fails to deliver valid data.

These three degrees of freedom, however, lead to an overparametrisation of the two-dimensional position information.

Naming the 3 *dependent* coordinates of the layers u, v, and w, each of them can be determined following equation (3.1) for each layer respectively. Any set of two of these coordinates can then be used to determine x and y, giving rise to the six equations [22]:

$$
\begin{aligned}
x_{uv} &= u \\
y_{uv} &= \frac{1}{\sqrt{3}}(u - 2v)
\end{aligned}
$$

$$
\begin{aligned}
x_{uw} &= u \\
y_{uw} &= -\frac{1}{\sqrt{3}}(u + 2w)
\end{aligned}
\tag{3.3}
$$

$$
\begin{aligned}
x_{vw} &= v - w \\
y_{vw} &= -\frac{1}{\sqrt{3}}(v + w)
\end{aligned}
$$

In the case of all three layers yielding valid position information, the values for x and y can thus be determined in three different ways. Typically, if all layers match within a certain predefined limit, the mean value is taken as the final result, leading to an enhanced position resolution [22].

3.3 The Zeeman Slower

In order to get the ^{6}Li-atoms into the Reaction Microscope, a small oven containing the Lithium is mounted on the side of the experimental chamber. By heating up the oven to a temperature of around 370 °C, the Lithium atoms will evaporate isotropically, while their velocities follow a Maxwell-Boltzmann distribution. Thus, a certain fraction of the evaporated Lithium atoms will be able to enter the experimental chamber through a pipe and overlap with the centre of the Reaction Microscope, enabling the trapping of these atoms.

Since the trapping efficiency of a MOT depends on the initial velocity of the

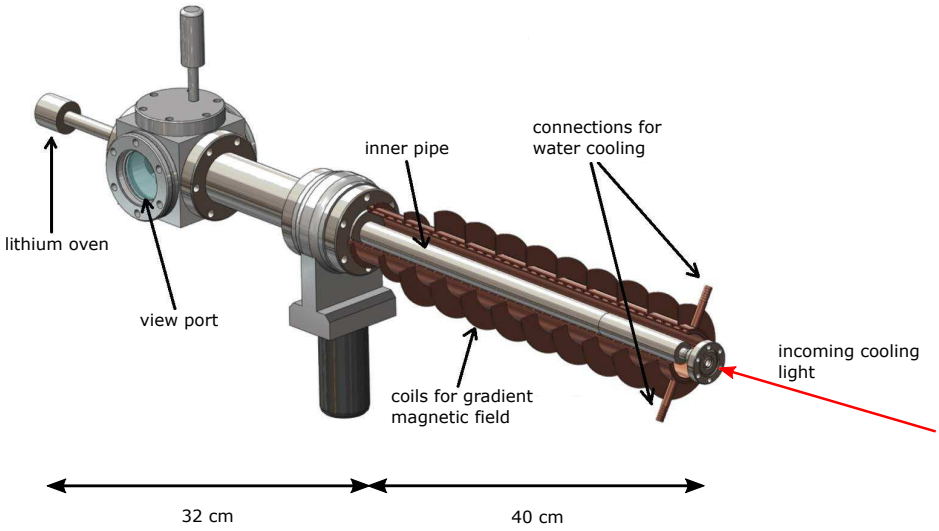

Figure 3.9: Technical drawing of the Zeeman slower used within the experimental setup of this thesis. The incoming light pre-cools the atom beam from the oven in order to increase the trapping efficiency in the magneto-optical trap. [6]

atoms, it is desirable to already slow the atoms down before they reach the trapping region of the MOT [6]. Within our experiment this has been realised by applying a so-called *Zeeman Slower* between the Lithium oven and the experimental chamber. A technical drawing of the slower can be seen in figure 3.9. It consists of a cooling light beam surrounded by coils which create a gradient magnetic field. As this, it is a one-dimensional application of the Doppler cooling principles described in chapters 2.1 to 2.3. Lithium atoms entering the chamber through the Zeeman Slower feel a spontaneous force, leading to a reduction in their kinetic energy, and thus, temperature. The Zeeman Slower used within the experiments of this thesis consisted of 10 single coils of different properties. The coils were supplied with the necessary voltages via remotely controllable *Zeeman Modules*, allowing for the turning

off of the magnetic Zeeman fields during experiments, where any external fields should generally be minimised in order to not distort the charged remnant particles.

3.4 Magneto-Optical Traps

A *Magneto-Optical Trap* (*MOT*) is a device used for trapping neutral atoms within a small volume by cooling them to very low temperatures, using the principles of laser cooling as described in chapters 2.1 to 2.3.
Only, in order to allow for cooling in all three spacial dimensions, a MOT usually consists of three pairs of counter propagating circularly polarised light beams, overlapping in the desired trapping region.
In order to realise this within the experiment, the beam from a single laser source has been split into three beams, all of which have been redirected to the experimental chamber. In order to create counter propagating beams of the correct helicity needed to cool the atoms (see chapter 2.3) each beam passed a $\frac{\lambda}{2}$-plate on the opposite side of the chamber, before being reflected back by a mirror, passing the $\frac{\lambda}{2}$-plate once more. Figure 3.10 shows a schematic of the MOT used within the experiment.

In order to confine the ^{6}Li-atoms in the centre of the Reaction Microscope, a gradient magnetic field is additionally necessary. For this purpose a quadrupole $\vec{B}$-field has been created by the use of an Anti-Helmholtz coil pair. A schematic of the field's profile in the yz-plane can also be seen in figure 3.10.
The cooling transition used for the MOT was the $|2^2S_{1/2}, F = 3/2\rangle \rightarrow$ $|2^2P_{3/2}, F = 5/2\rangle$ transition as shown in figure 3.11. However, since the allowed dipole transitions are given by $\Delta F = 0, \pm 1$ [15] and the atomic

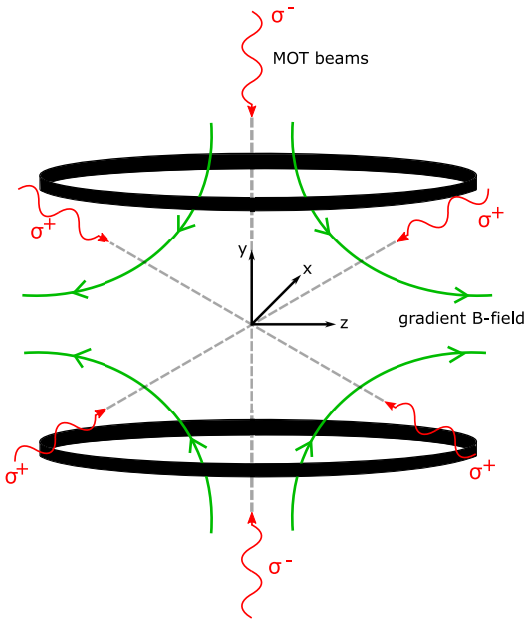

Figure 3.10: Sketch of the MOT used within the experimental setup. A pair of anti-Helmholtz coils (black) produces a quadrupole gradient B-field (green). In order to trap atoms in the MOT's centre, cooling light (red) from three spacial directions is being applied.

hyperfine structure energy levels are very close to each other, it is practically inevitable to excite to the $|2^2P_{3/2}, F = 3/2\rangle$ and $|2^2P_{3/2}, F = 1/2\rangle$ states as well. From these two states, a decay back to the $|2^2P_{1/2}, F = 1/2\rangle$ can occur, resulting in breaking of the cooling cycle. Therefore, in order to get any electrons from the $|2^2S_{1/2}, F = 1/2\rangle$ back into the cycle, a *repumper laser* has been applied to the MOT that gives rise to the transitions $|2^2S_{1/2}, F = 1/2\rangle \rightarrow |2^2P_{3/2}, F = 1/2\rangle$ or $|2^2S_{1/2}, F = 1/2\rangle \rightarrow |2^2P_{3/2}, F = 3/2\rangle$. In order to have a consistent cooling cycle, the repumper laser intensity was half the cooler laser intensity.

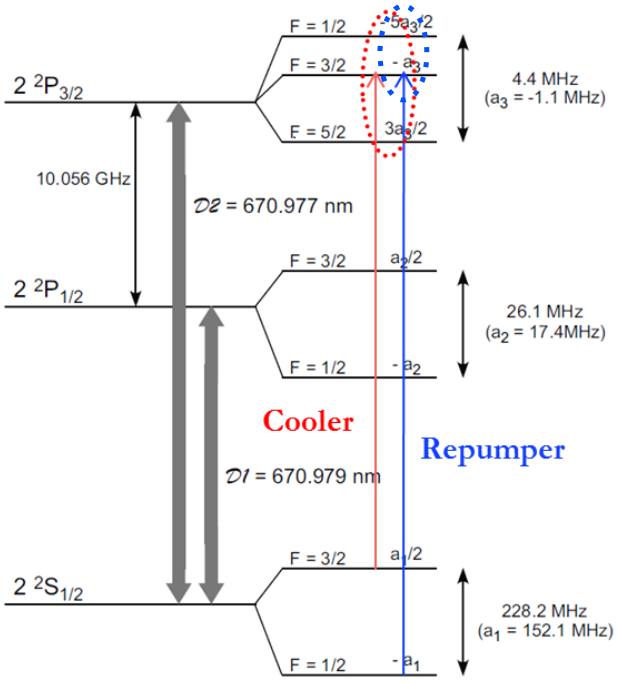

Figure 3.11: Cooler and repumper light transitions used within the experimental setup. In order to assure constant cooling, the repumper intensity was around half the cooler intensity. [14]

3.4.1 Fluorescence Imaging

In order to be able to see the atom cloud (MOT cloud) produced by the magneto-optical trap, a CCD camera has been mounted on one of the view ports of the experimental chamber. This camera allowed for the taking of pictures of the MOT cloud via *fluorescence imaging*, making it possible to obtain and deduce certain properties such as the cloud's shape, the number of atoms it contains, its temperature and more [5]. Figure 3.12 shows a typical image of the MOT obtained via fluorescence imaging.

Fluorescence imaging is simply realised by detecting the isotropically emit-

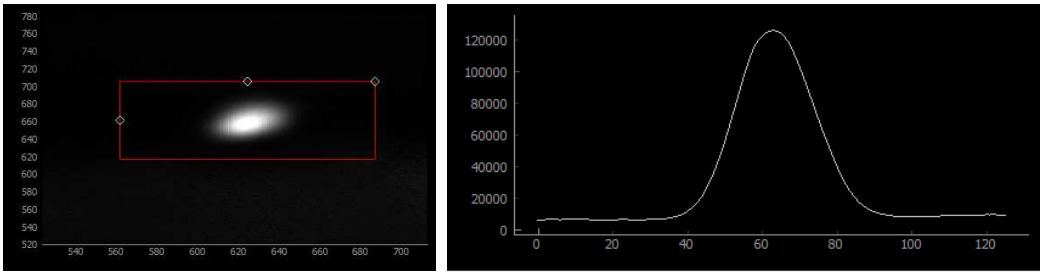

Figure 3.12: Left: Fluorescence Image of a MOT cloud taken by a CCD camera. Right: The corresponding sum of pixel counts projected on the x-axis.

ted photons of the MOT cloud due to the cooling cycle techniques used within the MOT (see e.g. chapter 2.1). Since the photons are emitted isotropically, a rather low fraction in the solid angle of the CCD camera can be used to produce an image.

An alternative method to fluorescence imaging is *absorption imaging*, a technique that allows for a better contrast of signal and background. When using absorption imaging, an imaging beam of the cooling transition's wavelength is applied to the atoms and the absorbed photon number is compared to the background without any trapped atoms. The CCD counts are then pixel-wise divided and the logarithmus of the obtained ratio is taken, giving an image of the optical density. This way, it is possible to achieve an image of the "shadow" that the atomic cloud casts on a CCD camera. While this method was succesfully applied in this thesis's experimental setup for imaging of the MOT cloud, an absorption imaging of optically trapped atoms in a dipole trap was not yet realised.

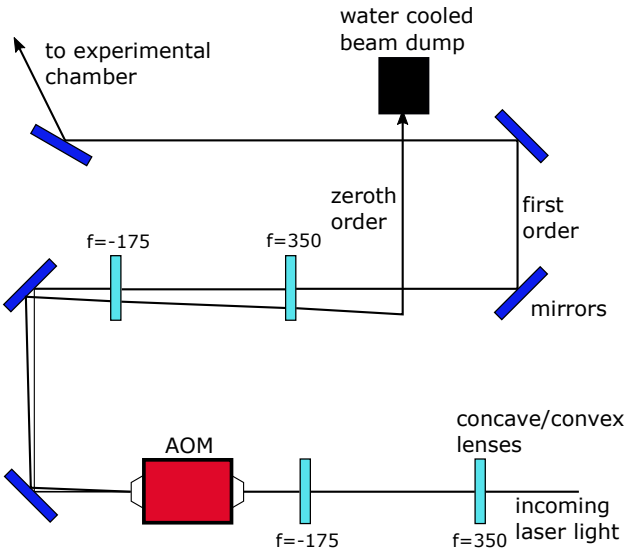

Figure 3.13: Dipole laser setup outside the experimental chamber.

3.5 The Dipole Laser

As for the dipole trap, an IPG Lasers YLR-Series single-mode CW Ytterbium Fiber Laser with a central wavelength of 1070 nm has been used. This is far red-detuned with respect to the cooling and repumping transition at around 671 nm, see also chapters 2.7 and 3.4. The laser light provides a light field of a Gaussian profile with a diameter of around 5 mm, a low divergence of around 0.3 mrad and has a maximum power output of 200 W that can remotely be adjusted to lower values. The exact setup for the dipole laser can be seen in figure 3.13.

First, the light traverses a telescope with lenses of focal lengths $f = -175\,\text{mm}$ and $f = 350\,\text{mm}$ in order to reduce the beam diameter to around 2.5 mm. This is necessary for the beam not being too large for the active aperture of the followup *Acousto-Optic Modulator* (AOM) in the setup. After that, another telescope increses the beam diameter back to its original size, since this increases the trapping volume of the dipole trap. The AOM's first

order light is then used for the actual trapping of the atoms, as its intensity can easily and continuously be adjusted by applying different voltages to the AOM. The zeroth order is being separated from the first order and deflected into a special beam dump that needs additional external cooling since the power of the infrared laser is so high. Using several mirrors, the first order light is then redirected into the experimental chamber under an angle of 18° with respect to the x-axis in the xz-plane.
Overall, a maximum diffraction efficiency of around 75% in the AOM's first order has been achieved, thus leading to a maximum power of around 150 W for the trapping atoms in the dipole trap.
One smaller challenge for the setup of the dipole laser was to achieve a good beam profile of the AOM's first oder, while still having a good diffraction efficiency. By first roughly adjusting the AOM's position to the correct *Bragg angle* and then fine adjusting its alignment by making use of some alignment screws, the profile shown in figure 3.14 has been achieved after several attempts. For comparison, the initial output beam profile of the laser is shown in the same figure.

3.6 The Femtosecond Laser System

As for the projectile beam, a FEMTOPOWER femtosecond laser system providing ultra-short pulses and high peak intensities has been used.
The central wavelength is given by $\lambda = 790\,\text{nm}$, corresponding to a photon energy of $E_{ph} = 1.57\,\text{eV}$. The pulse duration was determined to be around $\tau = 30\,\text{fs}$. With an output power of 2 W at a repition rate of 4000 Hz, a pulse energy of around $500\,\mu\text{J}$ arises. The spectral width of the laser lies above 40 nm.

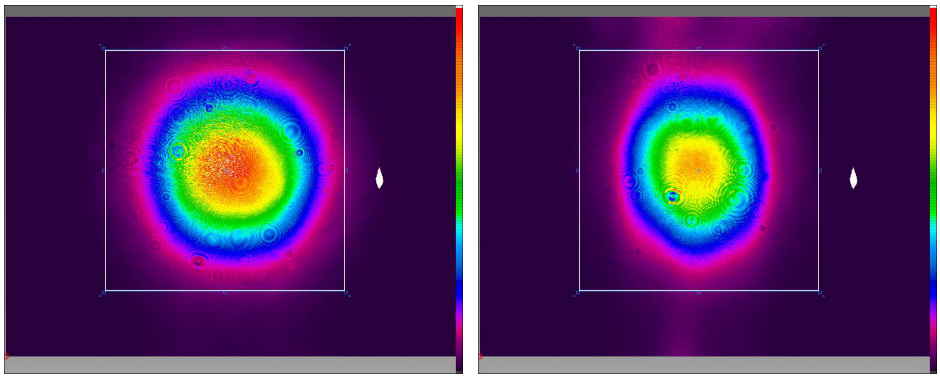

Figure 3.14: Left: Beam profile of the infrared dipole laser. Right: Beam profile of the first order beam behind the AOM used for trapping atoms in the dipole trap. The white spot on both pictures simply arises from broken pixels of the CCD camera.

4 Data Acquisition

This chapter's goal is to provide the necassary information on technical data and working principles of the data acquisition system used for the experiments.

4.1 Setup and technical Data

In order to calculate the positions and momenta of the incident particles it is necessary to obtain the corresponding time information of the signals induced on the detectors. For this purpose we use three CRONOLOGIC NDIGO5G highspeed ADCs, each of which consists of four available channels for independent processing of the different signals (MCP signals, delay line anode signals and a projectile trigger signal), after these have been amplified in ORTEC 995 Fast Amplifiers. While one of the ADCs is used for the projectile trigger signal and the two MCP signals from both detectors, the other two take care of the four layer signals of each detector, as shown in figure 4.1.

An important feature, different from common data acquisition setups used for Reaction Microscopes, is a further software-based processing of the incoming signals. Trigger conditions can be applied for each channel of the ADCs separately. In the case of the MCP and delay line signals, triggering on a certain negative threshold of a few mV on a falling slope has been used, while the trigger signal of the projectile needed a positive slope triggering. Over a period of 3.2 ns each channel takes four samples of the applied signal [23]. If a sample fulfills the required triggering conditions, the data is being recorded, leading to an uncertainty in time of $\delta t = 0.8\,\text{ns}$. Additionally, two parameters called *precursor* and *length* can be applied. While the precur-

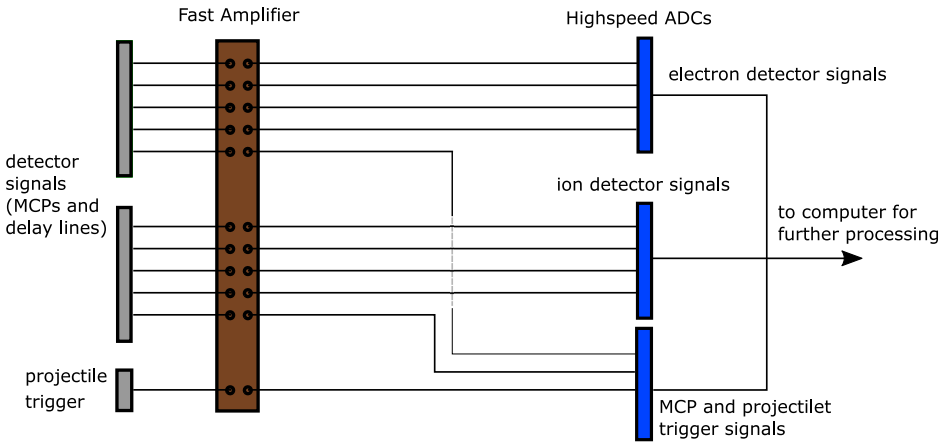

Figure 4.1: Setup of the data acquisition. The signals of interest get amplified in fast amplifiers before being sent to the highspeed ADCs. The obtained time information is then sent to a PC for further data analysis.

sor parameter leads to additional recording of data points before the trigger event, the length parameter enhances the time window of data recording after the trigger event. Both parameters are integer numbers that can only lead to increasement of the data acqusition time window in multiples of 3.2 ns [23]. Figure 4.2 gives an example signal with an additional explanation of the working principle behind the triggering on a channel.

Visually, whenever a trigger condition is met, the respective sample data of the signals are being connected, leading to curves as in figure 4.3. Every such data is recorded and comes additionally with a *time stamp*, giving the time of the trigger event. However, since the trigger event is solely depending on a specified threshold, the obtained relative time of the signals to the actual incidence of the particles will vary slightly from signal to signal as can be seen in figure 4.4. To prevent this, a function simulating a *Constant Fraction Discriminator (CFD)* is applied to a fit on the data, leading to a threshold independent time information by rather considering the time when a certain

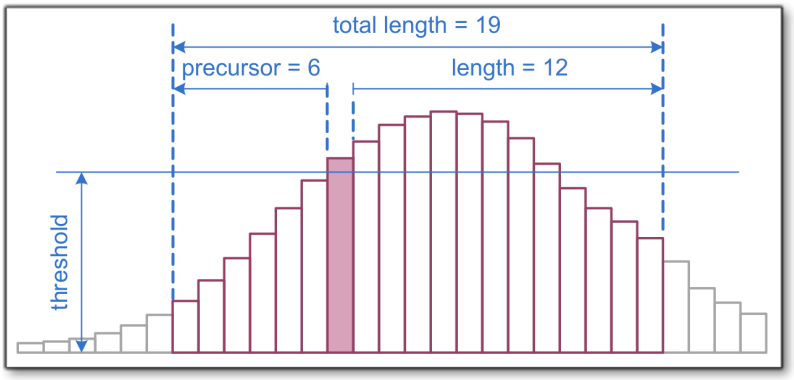

Figure 4.2: Working principle of triggering and data processing for the Ndigo5G Highspeed ADCs. When a certain threshold is exceeded, the data in a time window before and after the trigger event is being processed, corresponding to the parameters precursor and length. Each bin has a width of 3.2 ns and consists of four samples taken every 0.8 ns. [23]

ratio of the signal's maximum/minimum is reached. Figure 4.5 shows the general working principle of a CFD on an example Gaussian signal. As a software-based CFD function is used, the data acquisition setup requires no real hardware CFDs in order to obtain the correct time information and the uncertainty in time is reduced below 0.8 ns.

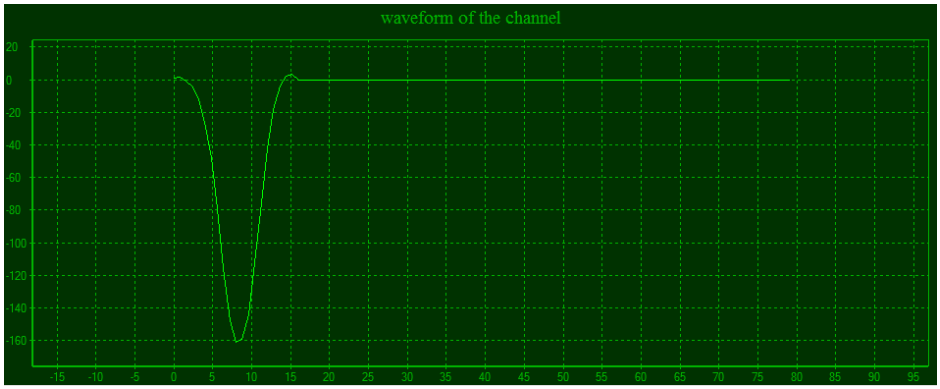

Figure 4.3: A typical MCP signal from a delay line detector. The y-axis is in units of mV, the x-axis in units of ns.

5 Data Analysis

The obtained raw data necessary for the computation of the involved particles' momenta consists solely of time information. During a measurement, this data can be stored for later analysis or immediately be processed and analysed using the software Go4. Go4 allows for an analysis of the experimental data, calculating the values of interest (momenta, angular distributions and so on) and providing histograms. Besides the possibility of giving a real time analysis of the experimental results, the Go4 software code can individually be adapted for one's needs.

In order to study and gain a deeper understanding of the ionisation processes taking place in a Reaction Microscope, the main goal is to reproduce the initial momentum distribution of the remnant particles involved in the reaction in question. Due to the cylindrical symmetry of the experimental setup, it is straightforward to define the momenta of interest as the *transversal momentum* $p_\perp$ and the *longitudinal momentum* $p_\parallel$ with respect to the spectrometer axis.

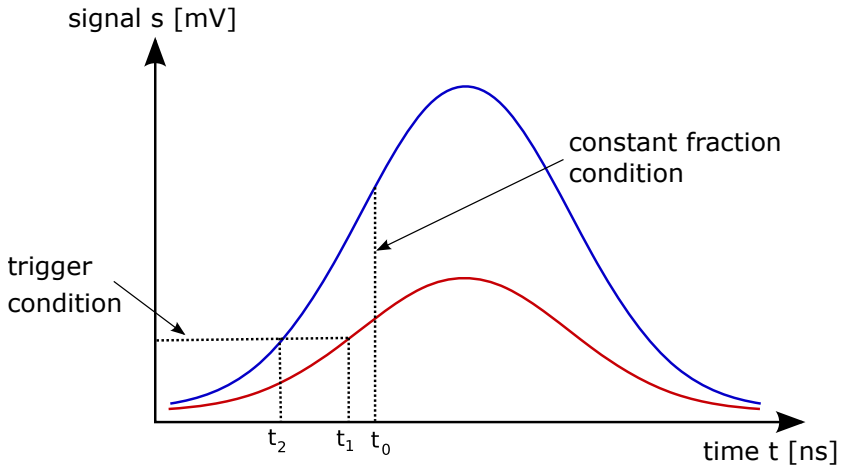

Figure 4.4: By applying simple threshold trigger conditions to the detector signals, the obtained relative times will depend on the signal amplitudes. This can be avoided by choosing a constant fraction trigger condition. [20]

5.1 Longitudinal Momentum

For each remnant particle of an ionisation process, the longitudinal momentum $p_{\parallel}$ can directly be computed by experimentally determining the time of flight t_{TOF} of the particle. t_{TOF} is defined as the time difference between the ionisation event itself t_{event} and the particle's arrival time on the MCP of the respective detector t_{MCP}, $t_{TOF} = t_{MCP} - t_{event}$. An example time of flight spectrum can be seen in figure 5.1.

In general, the time $t_{projectile}$, that corresponds to the trigger event of the projectile inducing the ionisation, differs from t_{event} due to the travel time from its source to the reaction volume. However, since only laser light has been used as projectiles during the course of this thesis, the travel time difference of just a few ns is neglectable in comparison to the overall time of

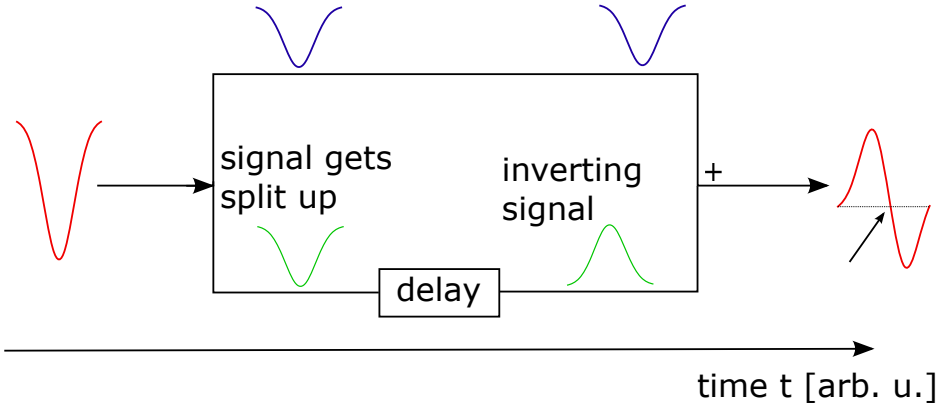

Figure 4.5: Basic working principle behind a constant fraction discriminator. An incoming signal gets split up, then one of the resulting signals is delayed and inverted. By adding the signals again, an amplitude-independent zero crossing results, corresponding to a constant fraction trigger condition. [20]

flight which typically lies at an order of magnitude of several μs for ions and several 100 ns for electrons. The experimentally determined time of flight is thus given by

$$t_{TOF} = t_{MCP} - t_{projectile} \tag{5.1}$$

Solving Newton's equations of motion, one finds that in a Reaction Microscope of acceleration length a and drift length d, with a coordinate system as shown in figure 3.2, the time of flight of a charged particle created at $z = 0$ is related to the longitudinal momentum $p_{\parallel} = p_z$ by the equation:

$$t(p_z) = m\left(\frac{2a}{\sqrt{p_z^2 + 2mqU} \pm p_z} + \frac{d}{\sqrt{p_z^2 + 2mqU}}\right) \tag{5.2}$$

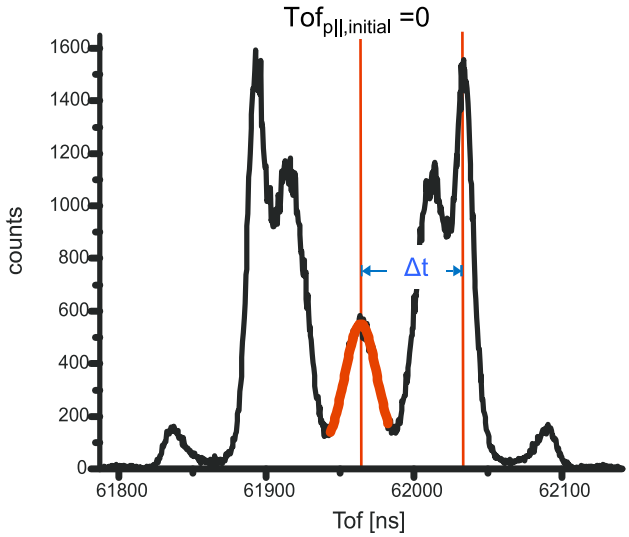

Figure 5.1: Example time of flight spectrum for ions. Typically, these ion spectra show symmetry around the time of flight for $p_z = 0$ and the linear approximation $\Delta t = \frac{a \Delta p_z}{qU}$ is applicable. [15]

Here, m, q, and U are the particle's mass, charge and the applied spectrometer voltage difference along the particle's path, respectively. The $+/-$ signs in equation (5.2) correspond to the formula for negatively/positively charged particles.

Equation (5.2) cannot be solved for p_z analytically, but by making use of Newton's method, as further explained in appendix B [22]. This method usually is applied for the data obtained from the electron detector. However, in the case of the much more massive ions, a linear approximation of equation (5.2), given by its Taylor expansion to first order

$$\Delta t_{TOF} = \frac{a}{qU} p \tag{5.3}$$

is typically sufficient, as has been used within this thesis. In this case, Δt_{TOF} refers to the time difference relative to the central time of flight for particles with initial longitudinal momentum $p_z = 0$, as shown in figure 5.1. This approximation cannot be used for the determination of electron longitudinal momenta, since due to their low masses and the non-linearity of equation (5.2), their time of flight spectra cannot be assumed to be symmetric around $p_z = 0$.

However, for photoionisation processes, the involved particles' momenta in z-direction will be distributed around $p_z = 0$. The respective theoretical central time of flight for $p_z = 0$ can then be directly found to be:

$$t_{TOF}(p_z = 0) = \sqrt{\frac{m}{2qU}}(2a + d) \tag{5.4}$$

Also, the time difference Δt between two momenta of same absolute value p, but opposite direction $p_z = \pm p$, can analytically be related via

$$\Delta t = \mp \frac{2ap}{qU} \tag{5.5}$$

This can be used for comparisons of theoretically expected values and experimental results.

5.2 Transversal Momentum

For the transversal motion of the ionisation particles, the magnetic extraction field produced by the Helmholtz coils around the Reaction Microscope has to be taken into account, since it induces a cyclotron motion of the particles

in the xy-plane via the *Lorentz force*.
The cyclotron frequency of this motion is given by

$$\omega_c = \frac{|q|B}{m} \tag{5.6}$$

Here, B is the strength of the magnetic field in z-direction. Typically, the exact magnetic field strength is not necessarily known, but the cyclotron frequency can be determined by plotting the radial positions of the particles $r = \sqrt{x^2 + y^2}$ against their time of flight. Since for each full cyclotron motion the particles will periodically be found at the same radial position, the time difference between two nodes as shown in figure 5.2 corresponds to one full period T_c and canbe determined with a precision of around 0.1 ns [22]. T_c can then easily be converted into the respective frequency ω_c:

$$\omega_c = \frac{2\pi}{T_c} \tag{5.7}$$

Furthermore, the cyclotron motion's *Larmor radius* R_c is directly connected to the particles transversal momentum $p_\perp = p_r$ via

$$R_c = \frac{p_r}{\omega_c m} \tag{5.8}$$

Note that the index r in this case denotes the *radial component*, not the *recoild ion* momentum.
Even though R_c cannot be measured directly, it is possible to take a look at the angle α in the xy-plane that a particle moves along the cyloctron trajectory, as shown in figure 5.3. With the experimentally obtained value

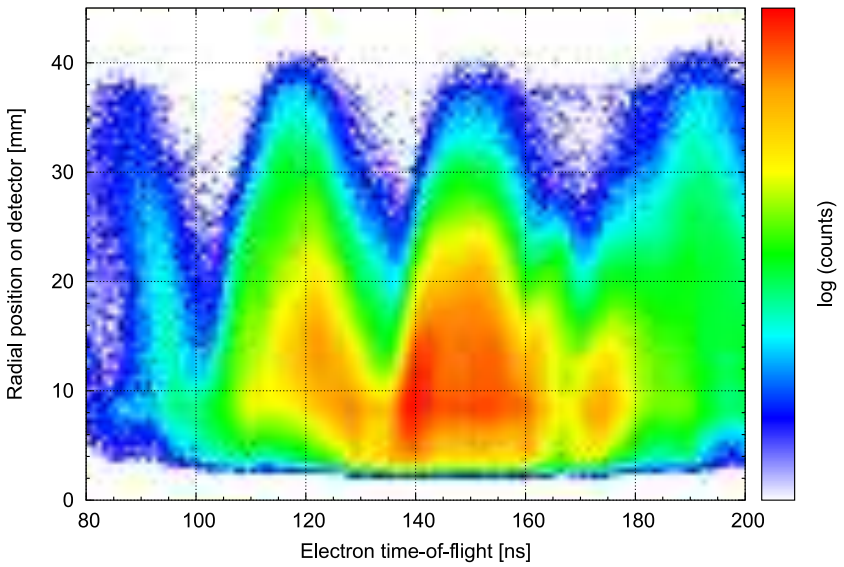

Figure 5.2: Radial position of electrons against their time of flight. The nodes occuring due to the cyclotron motion of the electrons can clearly be seen and experimentally determined. [22]

for ω_c, α can be computed to be

$$\alpha = \omega_c t_{TOF} \tag{5.9}$$

Considering that the particles' transversal momenta can be related to the experimentally determined positions and time of flights on the detectors by

$$p_r = \frac{mr}{t_{TOF}} \tag{5.10}$$

the Larmor radius can be expressed as

$$R_c = \frac{r}{2|\sin(\frac{\alpha}{2})|} \tag{5.11}$$

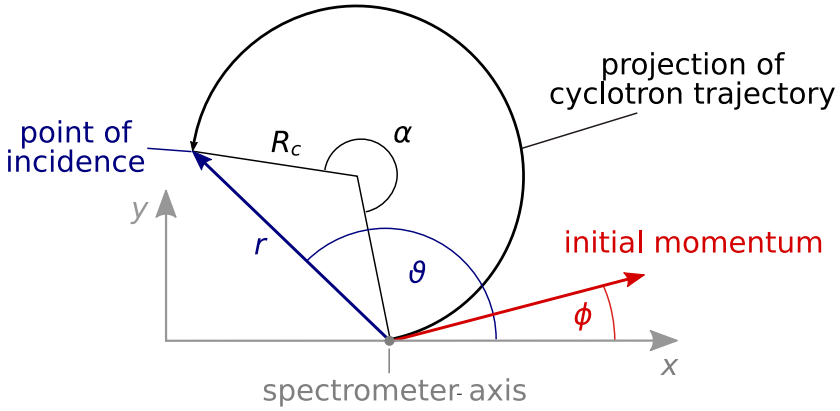

Figure 5.3: The different angles in the xy-plane resulting from the cyclotron motion of the particles. For ions the cyclotron motion is typically neglectable such that $\alpha = 0$ and $\vartheta = \phi$. [22]

Finally, inserting equation (5.11) in (5.8) leads to an expression that allows for experimental determination of p_r:

$$p_r = \frac{\omega_c m r}{2|\sin(\omega_c t_{TOF}/2)|} \tag{5.12}$$

While electrons will typically pass several cyclotron motions before they hit the detector due to their low mass and thus high sensitivity to external fields, in most cases the far heavier ions are barely affected by the magnetic field and their cyclotron motion can be completely neglected. In this limit of $\omega_c \to 0$, the transversal momenta of the ions can be calculated by the linear approximation

$$p_r = \frac{mr}{t_{TOF}} \tag{5.13}$$

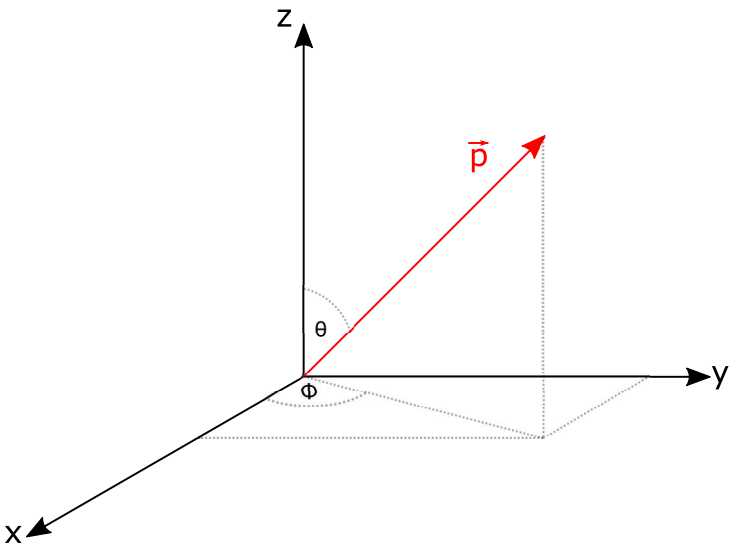

Figure 5.4: Angular coordinates of the particle momenta.

This also allows for the determination of the momenta in x and y direction independently, which is not possible for the electrons.

5.3 Angular Momentum Distributions

Additionally to the different spacial momentum components, their angular distributions around the spectrometer axis (see figure 5.4) can be of interest.

The azimuthal angle ϕ of a particle's initial momentum in the xy-plane can be determined from its point of incident on the detector with the knowledge of its cyclotron frequency and its time of flight. If ϑ is the angle between the vector pointing toward the particle's point of incidence and the x-axis as shown in figure 5.3, ϕ can simply be computed via

$$\phi = \pm\frac{\omega_c t_{TOF}(mod 2\pi)}{2} \tag{5.14}$$

Here, the $+/-$ signs correspond to *clockwise* and *counterclockwise* cyclotron motions, respectively. For ions with negligible cyclotron motion ($\omega_c \to 0$), one simply finds:

$$\phi = \vartheta = \cos^{-1}(\frac{p_x}{p_\perp}) \tag{5.15}$$

The polar angle θ can be determined from the momentum in z-direction p_z and the absolute momentum $p = |\vec{p}|$ via the equation:

$$\theta = \cos^{-1}(\frac{p_z}{p}) \tag{5.16}$$

6 Experimental Results

The following chapters will present the results from multiphoton ionisation experiments performed during the course of this thesis. All relevant information on the target, projectile and measurement procedure will be given and the obtained momentum distributions will be presented and discussed.

6.1 Multiphoton Ionisation from the Dipole Trap

In the following, the first results of multiphoton ionisation of ^{6}Li from an optical dipole trap will be presented.

6.1.1 Projectile Properties

For multiphoton ionisation from the dipole trap, the same femtosecond projectile laser system has been used as described in chapter 3.6, providing ultra-short pulses of a length of around $\tau = 30\,\text{fs}$ at a repitition rate of $\nu_{rep} = 4000\,\text{Hz}$ and a central photon wavelength of $\lambda = 790\,\text{nm}$, corresponding to a photon energy of $E_{ph} = 1.57\,\text{eV}$. The beam has been adjusted to be linearly polarised in direction of the y-axis by using a $\lambda/2$-plate followed by a polarising beam splitter. This setup also allowed for adjustment of the incoming laser intensity by rotating the polarisation angle on the $\lambda/2$-plate. Before entering the experimental chamber, the femtosecond laser beam traversed a focussing lens with a focal length of $f = 400\,\text{mm}$. While the original beam had a diameter of around 2.5 cm, the waist of the focus has been around $16\,\mu\text{m}$.

In order to assure an optimal overlap of the focus with the target atoms in the centre of the experimental chamber, the alignment of the beam and the

position of the lens have iteratively been adjusted by looking at the ionisation event rates from a MOT. At first, the count rate has been maximised for full power of the laser. For high powers, however, the focal volume can lead to ionisation over a larger region due to the spacial distribution of the laser peak intensities. Thus, the laser intensity has been ramped down and the position of the focus has been adjusted to maximise the count rate again. This process has been repeated until a sufficiently low intensity has been reached, at which any change of the focus position led to a strong decrease in event rates, indicating a very precise overlap of the focus and the interaction volume.

Since this process has been applied by ionising Lithium atoms out of a MOT, the detuning of the cooling and repumper laser had to be adjusted such that it coincided with the detuning used in the experimental sequence. This led to a shift of the MOT position corresponding to the position of the optically trapped Lithium atoms.

6.1.2 Target Properties

Since the target ^{6}Li in this experiment was purely trapped in an optical dipole trap, all atoms of the ensemble have been in the $2^2S_{1/2}$ ground state, thus no momentum distributions from different state electrons are to be expected. In order to overcome the ionisation potential of $E_{IP} = 5.39\,\mathrm{eV}$, the absorption of at least four photons from the femtosecond laser is necessary, resulting in an excess kinetic energy of $E_{kin} = 0.89\,\mathrm{eV}$ or a corresponding absolute momentum of $p = 0.256\,\mathrm{a\,u}$.

Furthermore, the atom number and temperature of the atoms within the dipole trap are strongly reduced compared to ionisation from a magneto-

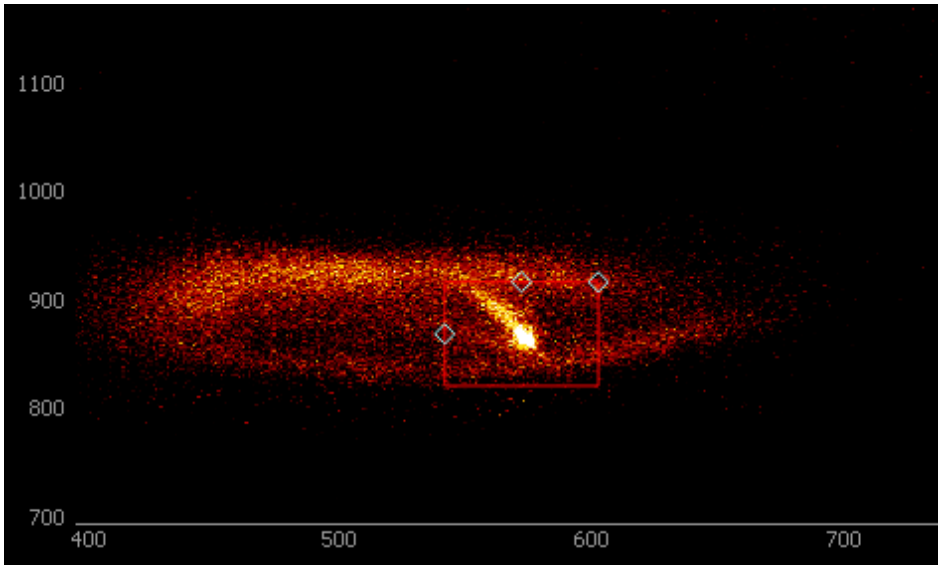

Figure 6.1: Example fluorescence image of optically trapped Lithium-6 atoms after a trapping time of 3 ms. The optically trapped atoms are clearly distinguished from the surrounding remnant atoms expanding from the MOT.

optical trap. While the temperature should in principal lead to a better momentum resolution, the reduced atom number leads to a reduced count rate, making long measurements of up to an hour a necessity in order to get an acceptable statistic. This, however, also depends on the applied intensity of the projectile beam.

Finally, figure 6.1 shows an example fluorescence imaging picture of atoms trapped in the dipole trap. Since the peak disappeared by blocking the dipole laser and running the trapping sequence, it could easily be confirmed that it shows optically trapped atoms.

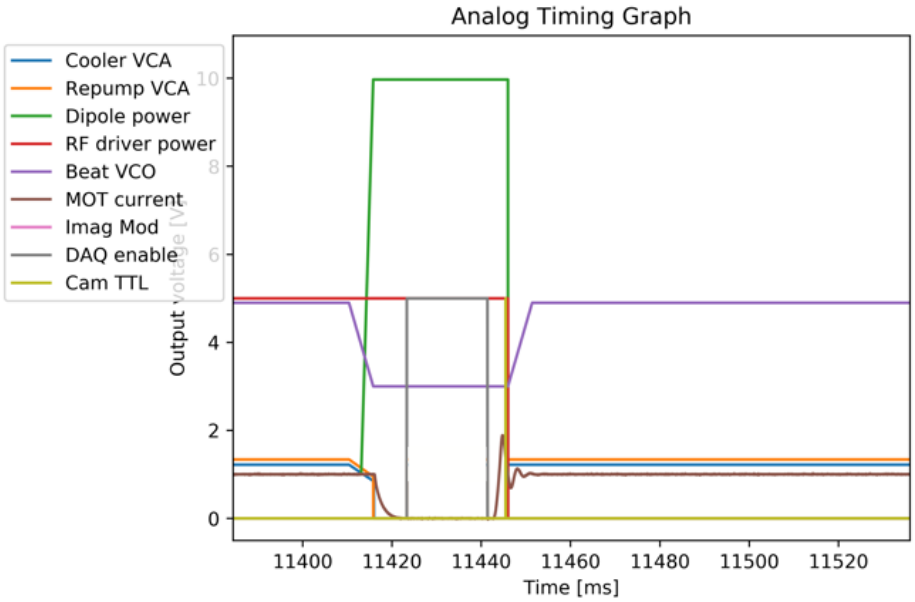

Figure 6.2: Example experimental sequence for ionisation of optically trapped Lithium-6 atoms in a dipole trap. The graph differs from the actual sequence used within the experiments described in the following chapters, since a trapping time of 5 s and other detuning values have been used.

6.1.3 Experimental Sequence

For the trapping and ionising of Lithium out of a dipole trap, a periodic experimental sequence has been applied to the experimental setup. Figure 6.2 shows an example sequence for low trapping times of atoms within the optical dipole trap.

First, the Lithium atoms coming from the oven have been loaded into the magneto-optical trap over a period of 10 s, before the MOT laser intensities Cooler VCA and Repump VCA were ramped down and turned off over period of around 10 ms. During this ramping, the Dipole Power was ramped to

its maximum and the detuning Beat VCO to a value of 2.55 V, slightly before the MOT coil current was turned off and the oven closed, releasing all atoms from the MOT and trapping the slowest atoms in the dipole trap. After 5 ms, in order to assure a completely vanished magnetic field from the MOT, the data acquisition has been turned on over the trapping time of 5 s. During this time, the ionisation of optically trapped Lithium-6 atoms was detected. After the data acquisition has been turned off, all conditions have been reset to enable MOT trapping once again, enabling repeating of the sequence until sufficient amounts of data have been obtained. In figure 6.2, RF driver power corresponds to the voltage supply of the AOM in the dipole laser setup (see figure 3.13) and Cam TTL is a TTL signal for the CCD camera, enabling fluorescence imaging. Imag Mod is used for absorption imaging, but was not considered in this sequence.

6.1.4 Results

In this chapter, the results of multiphoton ionisation experiments of ^{6}Li out of an optical dipole trap for five different femtosecond laser peak intensities ranging from $6.5 \times 10^{13}\,\mathrm{W/cm^2}$ to $6.5 \times 10^{14}\,\mathrm{W/cm^2}$ will be presented. Unfortunately, we were limited to this power range, since lower peak intensities led to a very slow count rate, while high intensities prevented the MOT from being loaded with Lithium during the loading process of the experimental sequence due to high ionisation rates. This, however, can and will be easily fixed by mounting a mechanical shutter in front of the femtosecond laser, blocking the beam during the loading of the MOT.

The applied extraction voltage on the reaction microscope's spectrometer over the whole 350 mm range of the acceleration regions was 15 V, from 7.5 V

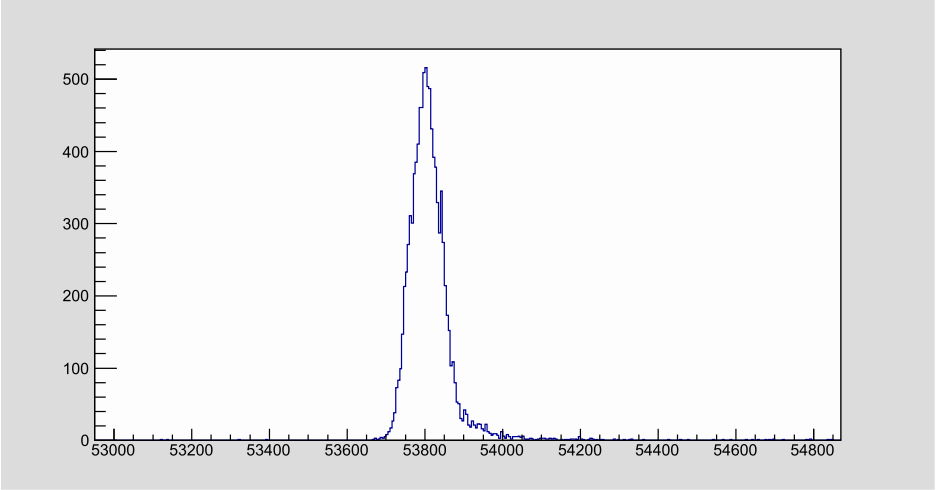

Figure 6.3: Time of flight distribution of ions from an optical dipole trap at an extraction voltage of 15 V. The y-axis corresponds to the number of counts in a bin, while the z-axis gives the time of flight in ns.

on the electron side to $-7.5\,\mathrm{V}$ on the ion side (compare with figure 3.2). This corresponds to an electric field of $E \approx 0.43\,\mathrm{V/cm}$, which is relatively low, but allows for a wider spreading of the transversal momentum of the remnant particles. The Helmholtz coils providing a homogeneous magnetic extraction field were turned off during all measurements. However, this should not affect the results, since only ions have been detected. Due to their relatively high masses, these are generally not very prone to distortions from magnetic fields.

Figure 6.3 shows a histogram of the obtained time of flights for the detected ions at a peak intensity of $3.39 \times 10^{14}\,\mathrm{W/cm^2}$. For all investigated intensities, the time of flight spectrum looked the same, showing a single peak at a central time of approximately $t_0 = 52.8\,\mu\mathrm{s}$, corresponding to ions of a transversal momentum of $p_z = 0$. Furthermore, the spectra show a slight asymmetry, as there appears to be some sort of "tail" in the distributions toward higher

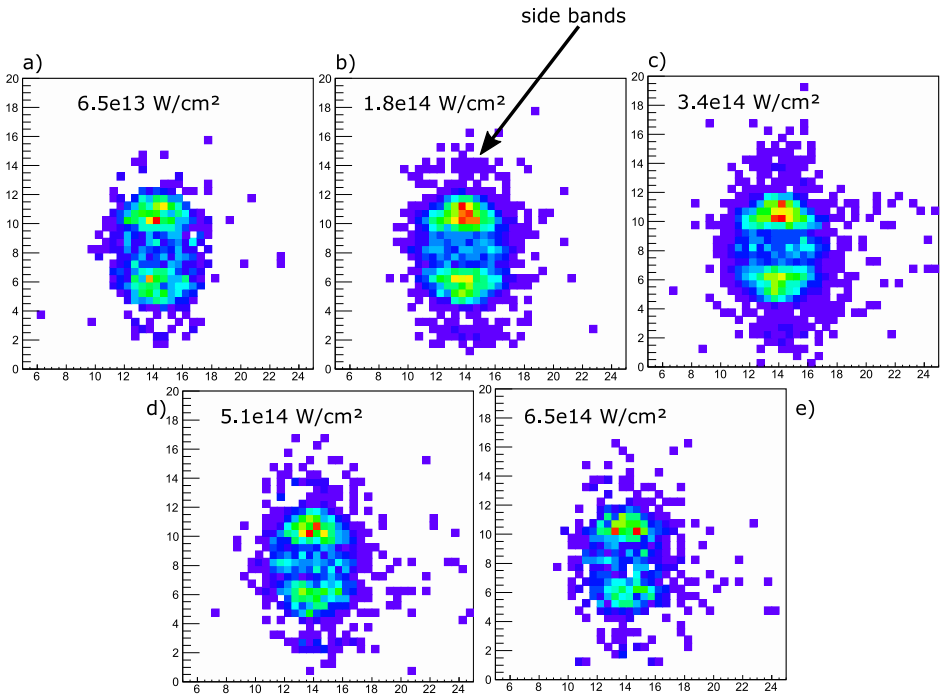

Figure 6.4: Position distributions of ions from the optical dipole trap. Both axes are given in mm and the colours indicate the numbers of hits within a bin, red being the highest and violet the lowest.

time of flights. While the origin of this effect remains unclear, it is for now assumed that it is not of physical relevance for the investigated ionisation processes, but rather a systematic artefact of the experimental setup.
While the time of flight yields the ion momenta in z-direction (see equation 5.3), their incident positions on the delay line anodes give rise to the transversal momenta, following equation 5.13. Thus, it is instructive to take a look at the position distributions as shown in figure 6.4.

As one can see, the position distributions show two lobes in $\pm y$-direction and a central hit region elongated along the x-axis. These three distinguished regions appear to be separated by two minima that become more pronounced for higher peak intensities of the laser. These results are consistent with the

polarisation of the femtosecond laser, as it was set up to be along the y-axis. Since the polarisation axis of the projectile laser is the only distinguished axis in this setup, a radial symmetry in the xz-plane perpendicular to the y-axis is to be expected.

Additionally, especially in figure 6.4 b), but also for higher peak intensities, some sort of side bands can be seen around the globes in the $\pm y$-direction. While these side bands could principally occur due to interaction of the dipole laser with the ions (which is also polarised in y-direction), the spacial separation from the globes is too big for a single dipole laser photon to induce such a large momentum change. Thus, they probably occur due to above-threshold ionisation of the atoms from femtosecond laser photons. In this case, the spacial separation is consistent with the additional momentum of a photon within the uncertainty in the spacing of the side bands of around 1 mm. Furthermore, the dipole laser intensity of around $1 \times 10^6\,\mathrm{W/cm^2}$ is not sufficient for absorption of photons from the dipole laser.

In figure 6.5 the ion momenta in y-direction p_y are plotted against their momenta in z-direction p_z, corresponding to the peak intensities as in figure 6.4. Only momenta for which the condition $|p_x| \leq 0.1\,\mathrm{a\,u}$ was fulfilled have been plotted in figure 6.5, thus integrating over less p_x values and giving rise to a clearer picture. In 6.5 b), a white circle shows where the obtained values should theoretically lie ($0.256\,\mathrm{a\,u}$), following the considerations of chapter 6.1.2.

One can see that the obtained momenta are consistent with the theoretically obtained value within. They are also consistent within the momentum resolution, as will be shown in the following chapter. Furthermore, in figure 6.5 some already mentioned features can be seen, such as a globe structure with two large maxima in positive and negative y-direction as well as two smaller

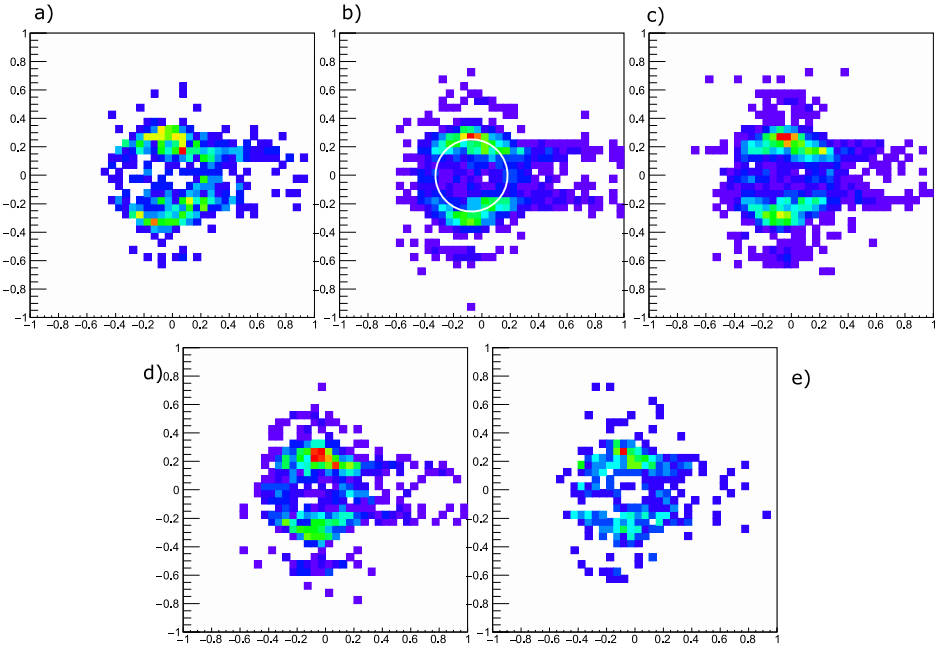

Figure 6.5: Ion p_y-momentum against ion p_z-momentum for $|p_x| \leq 0.1\,\mathrm{a\,u}$ in atomic units. The white circle in b) indicates the theoretical value for the absolute ion momentum $p = 0.256\,\mathrm{a\,u}$.

lobes in z-direction, e. g. the the majority of electrons/ions gets ejected in $\pm y$-direction, while only a smaller fraction has pure ejection in z-direction. Furthermore, the "tail" as seen in figure 6.3 can be seen, as each of the plots shows some tail counts toward positive p_z values.

Since four-photon ionisation from the $2^2S_{1/2}$ ground state leads to a mix of s-wave, d-wave and g-wave electron emission patterns (see figure 6.6), the different contributions can be found in the final momentum distributions. The smaller lobes at $p_y = 0$ and $p_z \approx \pm\, 0.256\,\mathrm{a\,u}$ that can clearly be seen in figures 6.5 b) to d), indicate a strong d-wave contribution to the final momentum states at the respective peak intensities, while in a) no smaller lobes can clearly be distinguished. Since the statistics for image e) were really low

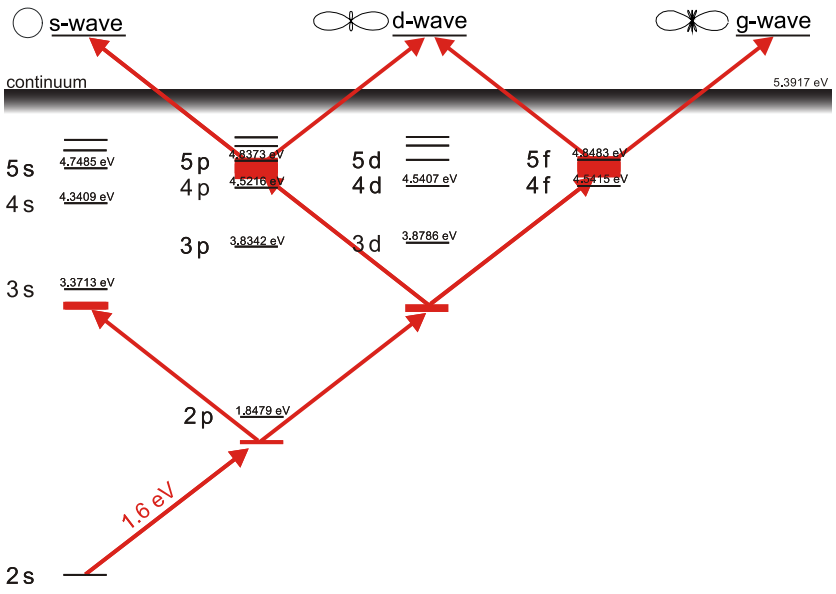

Figure 6.6: Possible emission patterns arising from multiphoton ionisation of Lithium-6 from the ground sate with four photons. The patterns show the angular momentum distribution patters around the polarisation axis of the projectile laser light. A larger distance from the distribution centre corresponds to a higher emission probability in the respective direction. [3]

due to the high atom loss during the MOT loading time, a real statement cannot be made, but the d-wave lobes seem to be slightly visible. In none of the images, however, any clearly distinguishable g-wave contributions can be identified, which would show themselves as additional distinguished maxima on the $p = 0.256\,\mathrm{a\,u}$ circle.

Finally, figure 6.7 shows the momenta transversal to the polarisation axis $p_\perp$ plotted against p_y. Since a radial symmetry around the y-axis is expected, these plots give complete information on the electron/ion momentum distributions. They are consistent with earlier observations and show three distinguished regions on the $0.256\,\mathrm{a\,u}$ sphere, corresponding to the lobes arising

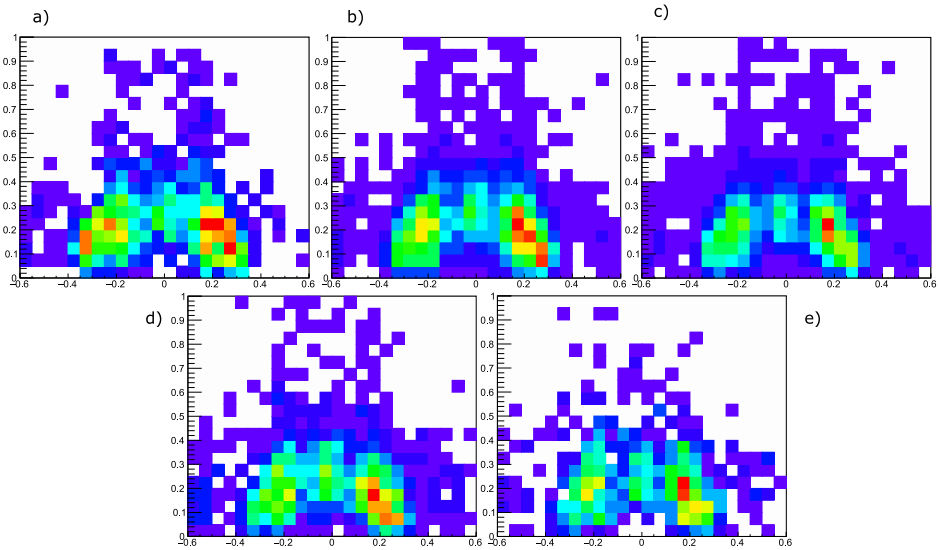

Figure 6.7: Ion $p_\perp$-momentum in xz-plane against ion p_y-momentum in atomic units.

from the d-wave contributions of the electorn emission pattern.
Comparing with results obtained by SCHURICKE [24], more strongly distinguishable g-wave contributions would have been expected in figure 6.7. However, the momentum distributions achieved in [24] were much better.

6.1.5 Momentum Resolution

It is important to get an estimate for the obtained momentum resolutions during the multiphoton ionisation experiments. In order to do this, one has to take another look at the momentum distributions shown in figure 6.5. By projecting out only p_y-momenta for which p_z fulfill a certain conditon (in this case $|p_z| \leq 0.1\,\mathrm{a\,u}$, it is possible to obtain a narrow p_y momentum distribution corresponding to the width of the sphere on which the momenta lie, as shown in figure 6.8.

By simply fitting a Gaussian function to one of the projected peaks, it is

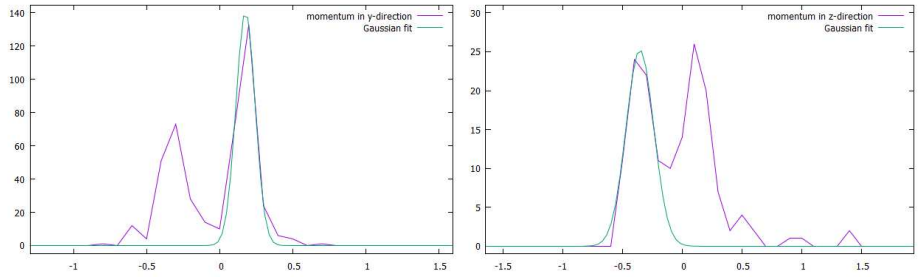

Figure 6.8: Left: Ion p_y distribution for small p_x and p_z. Right: Ion p_z distribution for small p_x and p_y. The units of the x-axis are given in a u

possible to obtain an estimate for the momentum resolutions in both directions, corresponding to their full width at half maximum (FWHM):

$$\begin{aligned} \Delta p_y &= 0.15\,\mathrm{a\,u} \\ \Delta p_z &= 0.27\,\mathrm{a\,u} \end{aligned} \tag{6.1}$$

While better resolutions should principally be able to be achieved, the obtained values are still acceptable.

7 Conclusion and Outlook

In this thesis, the first experimentally obtained final momentum distributions for multiphoton ionisation of purely optically trapped Lithium-6 atoms have been presented.

The experiments have been carried out in a MOTRemi setup, combining a magneto-optical trap and a Reaction Microscope. Initially, the target atoms have been trapped in a MOT, before being transferred into the dipole trap by applying a strong far red-detuned dipole laser. From this point, trapping of the atoms for several seconds was achieved, during which a femtosecond laser with peak intensities rangin from $6.5 \times 10^{13}\,\mathrm{W/cm^2}$ to $6.5 \times 10^{13}\,\mathrm{W/cm^2}$ has been used as projectile for the ionisation experiments. The main advantages of optical dipole traps are the absence of an additional magnetic field, the ability to achieve far lower temperatures compared to a MOT (down to around a few nK) and the absence of any mix states in the atomic target, since all Lithium-6 atoms were in the $2^2S_{1/2}$ ground state.

The obtained final ion momentum distributions as shown in figures 6.5 and 6.7 are consistent with formerly obtained results from multiphoton ionisations of Lithium-6 out of magneto-optical traps (see e. g. Schuricke [24] and Steinmann [5]). Clear favourised emission in direction of the polarisation of the projectile beam has been observed, as well as small lobes corresponding to the d-wave emission patterns of the photoelectrons perpendicular to the polarisation axis. While stronger g-wave contributions could principally also be expected, they could not have been identified. The main reason for this might be the rather low momentum resolutions $\Delta p_y = 0.15\,\mathrm{a\,u}$ in direction of the polarisation axis and $\Delta p_z = 0.27\,\mathrm{a\,u}$ in z-direction, perpendicular to the polarisation axis. Additionally, side bands occuring from above-threshold

ionisation were identified, especially good to see in figure 6.5 b).

Overall, the experimental results were rather limited in their statistics due to relatively low count rates in the investigated intensity ranges. For lower intensities, the count rates simply dropped due to less multiphoton ionisation events. For higher intensities, on the other hand, the reloading of sufficient atoms into the MOT and subsequently into the dipole trap was suppressed due to high multiphoton ionisation rates. The latter problem can easily be fixed by applying a shutter to the setup, blocking the femtosecond laser during the loading of the MOT in the experimental sequence described in chapter 6.1.3. Unfortunately, due to technical problems, delays occured that prevented further investigation on multiphoton ionisation of optically trapped Lithium-6 atoms within this thesis.
However, the results obtained and knowledge gained during the course of this thesis offer a good fundament for more precise and technically advanced experiments on optically trapped Lithium-6 atoms.

Besides trying to achieve further and more precise experimental results on the multiphoton ionisation of optically trapped Lithium-6 for a wider range of projectile peak intensities, there are several projects planned, building up on this work, the next steps being the additional detection of the emitted photoelectrons and the implementation of absorption imaging for optically trapped atoms.
Furthermore, evaporative cooling of the ^{6}Li atoms in order to achieve very low temperateues for the production of quantum degenerate gases is an exciting goal for the future, as in combination with the implementation of Feshbach coils to the experimental setup it will allow for many interesting experiments

with Feshbach Resonances and more.

Appendices

A Physical Constants and Unit Conversion

Property	Symbol	SI Units	Natural Units	Atomic Units
Boltzmann Constant	k_B	$1.3806 \times 10^{-23}\,\mathrm{J/K}$		
Speed of Light	c	$2.997\,924\,58\,\mathrm{m/s}$	1	1
Electron Mass	m_e	$9.109 \times 10^{-31}\,\mathrm{kg}$	$510.999\,\mathrm{keV}$	1
Elemental Charge	e	$1.602 \times 10^{-19}\,\mathrm{As}$	1	1

Table A.1: Table of physical constants used within this thesis in SI units, natural units and atomic units.

Property	Symbol	Atomic Units	SI Units	Natural Units
Mass	m	$1\,\mathrm{a\,u}$	$9.109 \times 10^{-31}\,\mathrm{kg}$	$510.999\,\mathrm{keV}$
Energy	E	$1\,\mathrm{a\,u}$	1	1
Charge	q	$1\,\mathrm{a\,u}$	$1.602 \times 10^{-19}\,\mathrm{As}$	1
Momentum	p	$1\,\mathrm{a\,u}$	$1.99 \times 10^{-27}\,\mathrm{kgm/s}$	$3.728\,\mathrm{eV}$

Table A.2: Conversion of some important observables from atomic units to SI units and natural units.

B Newton's Method

Newton's method is an iterative mathematical method for finding numerical solutions to non-linear equations. In order to be able to apply Newton's method, the function in question needs to be continuously differentiable at least once. For a function $f(x)$, the iterative formula for finding x such that $f(x) = 0$ is given by:

$$x_{k+1} = x_k - \frac{f(x_k)}{f'(x_k)} \tag{B.1}$$

Comparing with equation 5.2 shows that in order to find the correct value for p_z, $f(x)$ can easily be identified to be given by

$$f(p_z) = m\left(\frac{2a}{\sqrt{p_z^2 + 2mqU} \pm p_z} + \frac{d}{\sqrt{p_z^2 + 2mqU}}\right) - t \tag{B.2}$$

and the first derivative with respect to p_z is given by

$$f'(p_z) = m \mp \left(\frac{2a}{p_z^2 + 2mqU \pm p_z\sqrt{p_z^2 + 2mqU}} - \frac{dp_z}{(p_z^2 + 2mqU)^{3/2}}\right) \tag{B.3}$$

With these formulas, the numerical value for the longitudinal momentum p_z can easily be computed following equation B.1. However, an adequate starting value $p_{z(k=0)}$ and end condition $|p_{z(k+1)} - p_{z(k)}| \leq \mathit{condition}$ need to be chosen.

References

[1] Lars Heinen, Setup and Characterization of a Single-Focused Beam Optical Trap for Lithium, Bachelor thesis, 2017

[2] Harold J. Metcalf, Peter van Straten. Laser cooling and trapping. Graduate texts in contemporary physics. Springer, New York; Berlin; Heidelberg [u. a.], 1999

[3] Michael Schuricke, Multiphoton Ionization of Lithium, Diploma thesis, 2008

[4] Dieter Meschede. Optics, Light and Lasers. Physics textbook. Wiley-VCH, Weinheim, 2., rev. and enlarg. ed. edition, 2007

[5] Jochen Steinmann, Multiphoton Ionization of Laser Cooled Lithium, PhD thesis, 2007

[6] Christoph Bogda, Umbau und Inbetriebnahme eines MOTRemi-Aufbaus für zukünftige Experimente mit ultrakaltem ^{6}Lithium, Master thesis, 2015

[7] Michael Schuricke, Two and Three Photon Double Ionization of Lithium, PhD thesis, 2012

[8] X. Flechard et al., Kinematically Complete Charge Exchange Experiment in the Cs^+ + Rb Collision System Using a MOT Target, Phys. Rev. Letters 87.12, 2001

[9] S. Jochim et al., Bose-Einstein condensation of molecules, Science 302, no. 2101, 2003

[10] Renate Hubele, Kinematisch vollständige und zustands-selektive Untersuchung der stoßinduzierten Einfachionisation von Lithium, PhD thesis, 2013

[11] N. Delone, V. Krainov, Multiphoton processes in atoms, 2nd edition, Springer-Verlag, 2000

[12] R. C. Weast, M. J. Astle and W. H. Beyer, editors. CRC Handbook of Chemistry and Physics. CRC Press, Boca Raton, 64th edition, 1963

[13] I. Mills, T. Cvitas, K. Homann, N. Kallay and K. Kuchitsu. Quantities, Units and Symbols in Physical Chemistry. Blackwell Scientifig Publishing, Oxford, 1988

[14] Michael Eric Gehm, Preparation of an optically-trapped degenerate Fermi gas of ^{6}Lithium: finding the route to degeneracy, PhD thesis, 2003

[15] Renate Hubele, Implementation of an optical dipole trap for Lithium, Diploma thesis, 2009

[16] Johannes Goullon, One and two Electron Processes in Charge Transfer and single Ionisation in Ion-Lithium Collisions, PhD thesis, 2014

[17] Daniel Fischer, Aufbau eines Reaktionsmikroskops zur Untersuchung von Ion-Atom-Strößen, Diploma thesis, 2000

[18] Thomas Pflüger, Electron impact single ionisation of small argon clusters, Diploma thesis, 2008

[19] M. Lampton et al., Delay line anodes for microchannel plate spectrometers, Review of Scientific Instruments, vol. 58, no. 12, pp. 2298-2305, 1987

[20] Moritz Weegen, Ein Teilchendetektor für die Untersuchung atomarer Reaktionen, Bachelor thesis, 2015

[21] J. L. Wiza, Microchannel plate detectors, Nuclear Instruments and Methods, vol. 162, pp. 587-601, 1979

[22] Arne Senftleben, Kinematically complete study on electron impact ionisation if aligned hydrogen molecules, PhD thesis, 2009

[23] cronologic GmbH & Co. KG, Ndigo5G User Guide, Revision 1.0.7, 2017

[24] Michael Schuricke, Strong-field ionization of lithium, Phys. Rev. A 83, 023413, 2011

Erklärung

Hiermit versichere ich, dass ich diese Arbeit selbstständig verfasst und keine anderen als die angegebenen Quellen und Hilfsmittel verwendet habe.

Heidelberg, den 28.06.2018

Moritz Weegen